Hahn-Meitner-Institut
Berlin

Annual Report 2001
Selected Results - SE

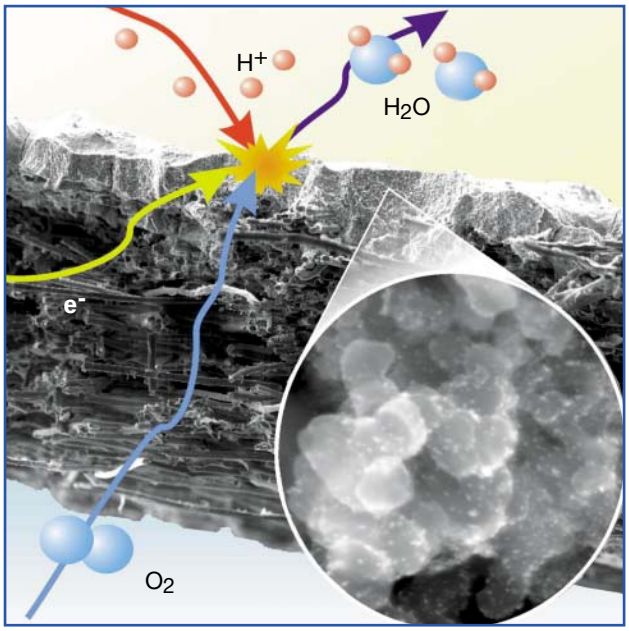

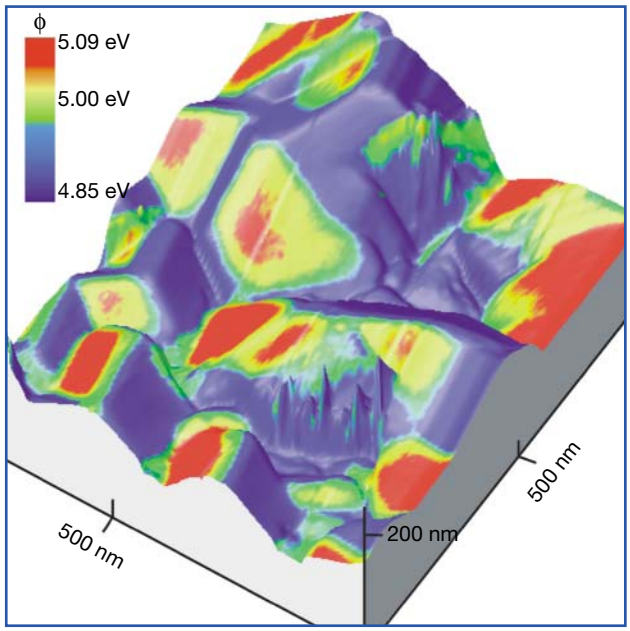

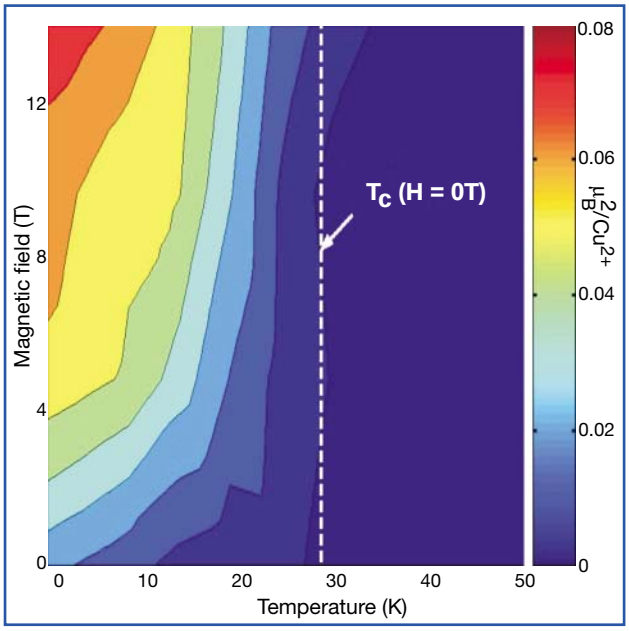

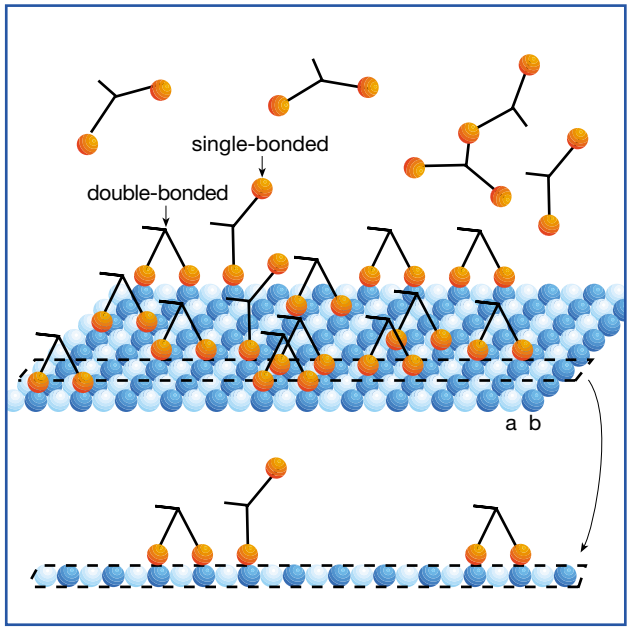

Hahn-Meitner-Institut
Berlin

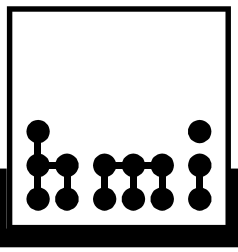

Annual Report 2001

Selected Results

Berlin 2002

Captions of cover images

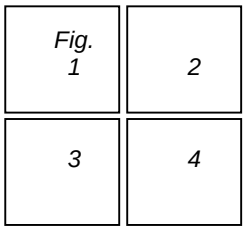

Fig. 1: SEM image of a gas diffusion cathode. The oxygen reduction occurs on catalytic nano particles which are incorporated into the high porous carbon black layer (enlarged insert).SE5.

Fig. 2: 3-dimensional representation of the surface of a $CuGaSe_2$ layer on a ZnSe(110) single crystal. The color scale represents the simultaneously measured work function using a Kelvin Probe Force Microscope. Differently oriented faces of single grains show different work function values. SE2.

Fig. 3: Neutron diffraction data for $La_{2-x}Sr_xCuO_4$ as a function of temperature and magnetic field. The figure shows the square of the ordered spin moment per Cu^{2+} ion as a function of temperature and applied magnetic field. The ordered moment squared is proportional to the observed neutron scattering signal. It first becomes significant below the zero-field superconducting transition temperature (T_c(H=0T)), and increases with decreasing temperature and increasing field. BENSC User Experiment performed with V2 (cold triple-axis-spectrometer).

Fig. 4: Schematic representation of the binding of kinesin dimers to a tubulin sheet. SF5.

1. Edition June 2002

Annual Report 2001
Selected Results
HMI-B 585

Hahn-Meitner Institut Berlin GmbH
Glienicker Str. 100
D-14109 Berlin (Wannsee)

Co-ordination:
Maren Achilles
Telefon: (030) 8062 2668
Telefax: (030) 8082 2047
e-mail: achilles@hmi.de

Table of Contents

Editorial

The scientific results from research and development of the Hahn-Meintner-Institute presented in this annual report give a representative inside into the activities and achievements of the last year, 2001.

Contributions are arranged along the departmental organization of the scientific divisions. Even though the results are of course based equally on the engaged work of the staff outside the scientific departments – from information technology over technical units to the administration. The activities directly connected to the user service at the large-scale facilities BER II / BENSC and ISL are summarized in separate chapters.

At the end of each text the reader finds a list of the responsible scientists as well as the project number and designation for internal purposes.

In addition to this annual report, HMI publishes a separate supplement, which contains the following statistical informations:

Listing of

- Publications
- Conference contributions and invited lectures
- Technology transfer and patents
- Academic education
- Co-operation partners and guests
- External funding
- Participation in external scientific bodies and committees
- Miscellaneous

Both the report and the separate supplement are available as download on the homepage of the Hahn-Meitner-Institute:

http://www.hmi.de/pr/druckschriften.html

or can be referred on request over the public relations office of the institute:

Hahn-Meitner-Institut Berlin GmbH
Öffentlichkeitsarbeit
Glienicker Strasse 100
D-14109 Berlin
e-mail: info@hmi.de

Annual reports covering various HMI activities in greater detail are

Statusbericht Strukturforschung 1997 – 2000
HMI-B 575

Status Report Solar Energy 1998 – 2001

BENSC Experimental Reports 2001
HMI-B 584

ISL Annual Report 2001
HMI-B 587

Foreword

With this report we present to the public selected results of the research and development activities in the Hahn-Meitner-Institute during the year 2001. We hope the reader will be convinced that at HMI cutting edge research was performed by both our own staff and the large community of external users of our facilities, and we are grateful for the boundary conditions and the resources setting the base for this success.

Looking at the activities in comparison to the past, programmatic re-orientations are getting visible. With Prof. Frey (SF5, Theory,,1.6.01) and Prof. Banhart (SF3, Materials, 1.1.02) distinguished representatives of the young generation took responsibility and are starting new scientific programs. This change of generation will continue with appointing new heads of the departments in both the divisions for Structural Research and Solar Energy Research in the near future.

It is important to underline that joint appointments with the universities remain key instruments to integrate the institute into its scientific surrounding. 2001 saw intensive discussions with the Humboldt-Universität and the Universität Potsdam to come to agreements similar to the most successful arrangements with both the Freie Universität Berlin and the Technische Universität Berlin. Final signing of cooperation agreements is scheduled for the summer of 2002.

In 2001, an important milestone was the very positive evaluation of the division for structural research based on the presentation of the results of the last four years to the Scientific Council, approving the programmatic strategy of the division and in particular the strong engagement in the user service at BENSC and ISL as one of the prime tasks of HMI as a Helmholtz Research Center.

Motivated by the rising request of the “bio-soft”-community for dedicated instruments at BENSC, work started to erect a new hall to house additional neutron instruments using the cold neutron source.

Even more challenging are the plans to further push the world-wide leading position of BENSC in providing highest magnetic fields for studying samples by neutron scattering. HMI proposes to install a High Magnetic Field Laboratory for Neutron scattering, NMFL, where fields up to 40 Tesla can be realized for neutron experiments. Conventional magnet technology will be combined with new technologies for neutron guiding and neutron detection both invented at HMI. NMFL is one out of nine projects of the next generation of large scale facilities for the sciences, presently evaluated by the German Wissenschaftsrat.

Another of these nine projects is the European Spallation Source ESS, where HMI acts as the leading laboratory to propose and develop the most suitable instrumentation.

The evaluation of the Solar Energy division is due for Spring 2002. Here also the long – term strategy of the division and the scientific orientation of upcoming joint appointments will be on the agenda.

Both scientific divisions took very successful efforts to use the potential of Berlins third generation source of synchrotron radiation, BESSY, for its scientific program. In a very fruitful collaboration with BESSY two especially designed insertion devices and several beam lines in 2001 could be pushed to near completion. First experiments are scheduled still before end of 2002. In 2001 the HMI staff working at BESSY could also move into a newly erected building at the BESSY site in Adlershof.

All these projects as well as all the achievements of last year are based on and depend upon the dedicated work of our staff and the user community of our facilities. Equally important is the steady support of our advisory boards and our funding agencies. Our thanks go to everybody for his share to keep and develop HMI as a place to do cutting edge science well noticed on the national and international scale.

On this basis we also feel well prepared to face the new scheme of program oriented funding of the HGF. We are confident that HMI is well positioned for the challenge and will successfully face the competition initiated by the new funding.

Division

SE Solar Energy Research

The solar energy division of the HMI concentrates its research activities on the exploration of the potential of highly productive thin-film technologies for solar cells of „tomorrow“ and „beyond“. The main objective is to realize systems which lead to substantial cost reduction at high conversion efficiency. This requires research for improvements of materials and systems which are already at the edge of being industrialized but also research for new materials and innovative solar cell structures. Therefore, the activities reach from basic material research to the development of technologies for solar cells and minimodules on the laboratory scale.

The work is supported by the broad range of analytical methods available in both sections of the HMI, particularly in the field of surface and interface physics, defect spectroscopy, ion-beam techniques and structural characterization, solid states physics, as well as conventional material and device analysis.
The groups collaborate in numerous projects and networks with national and international partners.

The division Solar Energy Research comprises 5 scientific departments:

SE1	**Silicon Photovoltaics**
SE2	**Heterogeneous Materialsystems**
SE3	**Technology**
SE4	**Dynamics and Interfacial Reactions**
SE5	**Solar Energetics**

and the group

SE6	**Electronic Structure of Semiconductor Interfaces.**

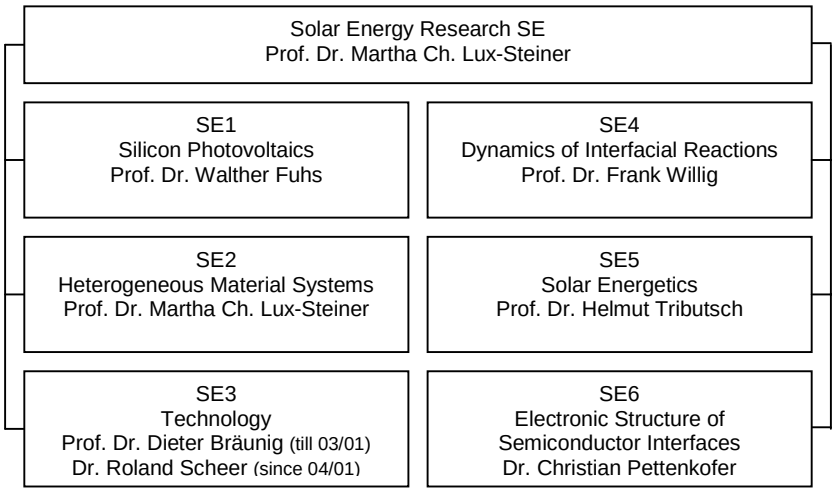

Department

SE1 Silicon Photovoltaics

Pulsed EDMR – New insight into the mechanisms of recombination in thin crystalline silicon films

The characterization of materials for photovoltaic applications depends strongly on methods that allow an assessment of electronic loss mechanisms. The major part of these losses are due to recombination processes of photogenerated charge carriers which are caused by localized bandgap states due to structural defects and impurities. The electronic activity of a certain type of defect is not only related to its density in a given material but also to its cross section which describes the probability for the capture of carriers into a defect state. Traditional methods of defect characterization are unable to provide microscopic information about such parameters for distinct defects. For instance, when the average charge carrier lifetime as well as the defect distributions in a material are known, it is still unclear which of the observed defects is more and which is less active without the knowledge of the respective recombination cross section and hence a systematic improvement of the photo response of a material becomes difficult.

An important part of the activity in our investigations of electron spin resonance (ESR) has therefore been the development of a new characterization method that combines the advantages of ESR, namely the microscopic identification of certain types of defects, with lifetime measurements of photogenerated charge carriers. The product of this development is the "Time domain measurement of spin dependent recombination" (TSR) [1-3], a method strongly related to electrically detected magnetic resonance (EDMR). The method bases on the fact that spin-selection rules determine the recombination probability between two paramagnetic states. For instance, the recombination rate between paramagnetic states that are initially in a triplet state can be by orders of magnitude smaller than between partners in a singlet state.

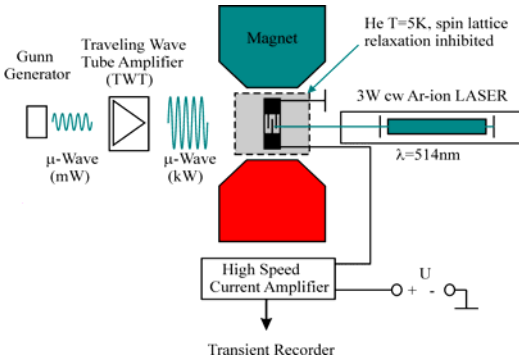

Fig. 1: The experimental principle of TSR: A semiconductor sample with micrometer-structured lateral Al-contact grids in an ESR microwave cavity is continuously exposed to strong LASER light. The transient measurement of the sample resistance after a fast (nanosecond) and strong (kW) ESR excitation of a certain defect type reveals the defects' distinct recombination cross section.

By applying intensive (kW-range) and very short (nanosecond–range) coherent microwave pulses at ESR resonance, the spin state of such recombining pairs can be rapidly altered at rates that are faster then any other process that may determine recombination, e.g., spin relaxation, pair creation as well as recombination or dissociation of electron-hole pairs. The microwave induced change of the spin states rapidly alters the recombination probability which may be observed as a time-dependent photocurrent change. The technical challenge of TSR lies in the implementation of an appropriate time resolution of the measured current changes. After employment of state-of-the-art current amplifier and transient recorder technologies as well as a special interdigited micrometer- structured sample contact system, it was possible to detect relative conductivity changes in the 10^{-8} range at time resolutions of less then 5 μs.

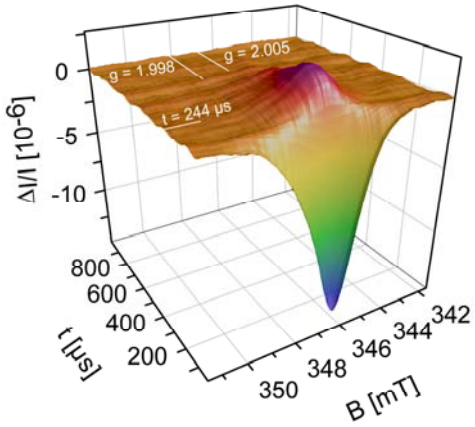

Fig. 2: In contrast to conventional EDMR, TSR not only identifies the states that are involved in recombination but also gives detailed information on their dynamics. The plot shows the time evolution of the ESR-induced current transients as a function of the magnetic field. The field dependence clearly reveals the involvement of dangling bonds (Landé factor g = 2.005) and band tail states (g = 1.998). The time dependence exhibits an initial strong current quenching followed by an enhancing.

As an example for the potential of TSR with regard to the characterization and investigation of recombination processes in semiconductors, the dynamics of recombination between shallow bandtail states (CE) and dangling bond (db) in hydrogenated microcrystalline silicon (μc-Si:H) is discussed in the following. A set of real-time TSR transients measured at various externally applied magnetic fields on a 2.7μm thin film of μc-Si:H is displayed in Fig. 2. The experiment was carried out at a sample current of I_{ph}=100μA. A 320ns pulse at time t = 0 leads to a strong recombination increase* at magnetic fields

* Since the current change ΔI is proportional to negative recombination change -ΔR, current decreases indicate recombination increases and vice versa.

which correspond to the ESR resonance of the CE and db states. After the current quenching signal relaxes, an enhancing signal becomes apparent which has a slower decay constant. Since the magnetic field dependences of the quenching and the enhancing effect are identical, we may conclude that both effects belong to the same recombination process.

As explained in previous publications [1,2], the pulse length dependence of a TSR transient can reveal the spin dynamics of the recombination centers during the resonant microwave interaction. Since microwave pulses can be changed in 2ns steps, the influence of coherent spin motion on recombination which has been predicted just recently [4], can be detected. The first results of this new high-resolution TSR indicate such a fingerprint of coherent spin motion of electrons and holes. The application of two 180° phase shifted 64ns resonant microwave pulses at times t=0 ns and t=64 ns induces a recombination echo a t=128 ns observed as a current spike shown in Fig. 3. By changing the timing of the two pulses the time evolution of the echo (echo decay) may be measured which contains all information on the dynamics of the recombination process.

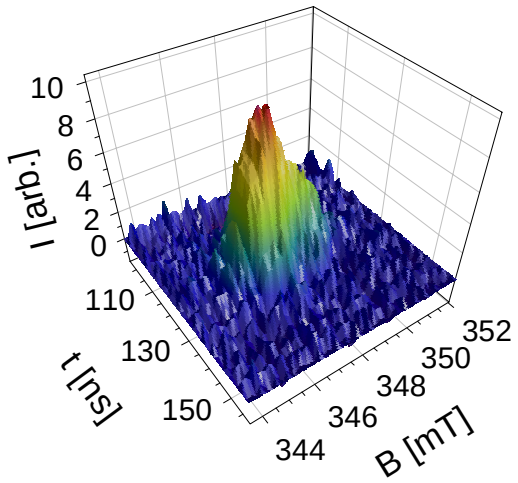

Fig. 3: Indirect TSR of a nanosecond microwave pulse shows the existence of an echo effect in the CE-db recombination rate of µc-Si:H. The current peak is caused by rephasing spins of recombining charge carriers and therefore is evidence for the influence of coherent spin motion on recombination. The recombination rate can be determined from the temporal behavior of the echo.

The fact that the shape of the recombination echo is the same for both quenching and enhancing signals, gives additional support of the fact that both belong to the same recombination process.
The observation that ESR changes of spin dependent recombination can lead to an increase of the photocurrent has never been proven experimentally although it was predicted theoretically for the finite triplet recombination probability. As illustrated qualitatively in Fig. 4, a non vanishing triplet recombination leads to a steady state population of the electron-hole ensemble where the triplet density is much higher than the singlet density, providing that the singlet recombination rate is larger than that of triplets. Under ESR resonance, both singlet and triplet densities are equalized which means that the singlet and triplet densities are enhanced and depleted, respectively leading to a net increase of the recombination. After the end of the ESR pulse, both singlet and triplet densities relax back to their steady state population. Due to the higher singlet recombination, this relaxation is faster for singlet states than for triplets. Therefore, the net recombination will shift temporarily below the steady state value which leads to an increase of the photocurrent (illustrated in Fig. 4 after about 250 µs for µc-Si:H).

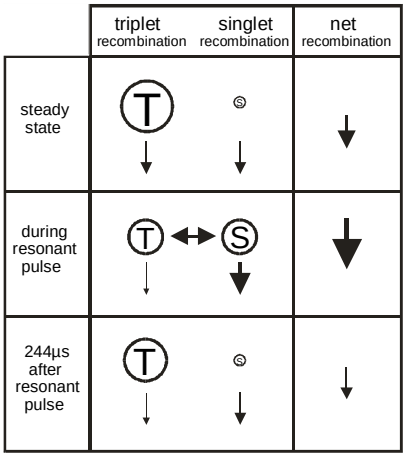

Fig. 4: Qualitative illustration of the dynamics of triplet -recombination. For details see text.

The prove of non-vanishing triplet recombination in µc-Si:H is of importance for the understanding of the recombination mechanism. Our measurements strongly suggest that the recombination cross sections can strongly be determined by spin-spin or spin-dipole interaction, which are related to bonding angles and topologies and hence depend on the microscopic structure of the material.

References
[1] Böhme, C.; Lips, K.:
Time domain measurement of spin-dependent recombination
Appl. Phys. Lett., 79 (26), 2001, pp. 4363-4365

[2] Böhme, C.; Kanschat, P.; Lips, K.:
Time domain measurement of spin-dependent recombination - a novel defect spectroscopy
Nucl. Instr. Meth. B, 186 (1-4), 2002, pp. 30-35

[4] Böhme, C.; Kanschat, P.; Lips, K.:
Quantum-beat recombination echoes
Europhys. Lett., 56 (5), Dec 2001, pp. 716-721

C. Böhme, K. Lips, W. Fuhs
(SE1.01a Crystalline Silicon Thin-film Solar Cells)

Amorphous/crystalline-silicon heterojunction solar cells

a-Si/c-Si heterojunctions are promising candidates for highly efficient solar cells processed at low temperatures. They are attractive as a low-cost alternative to the traditional Si wafer technology. As a bench mark Sanyo Corp. has reported on an efficiency of η=20.7 % for a laboratory cell based on this type of heterojunction with monocrystalline Si and has announced the production of modules of η=15.2 %. It is very interesting to use such low-temperature emitters also with low-cost Si substrates and in particular with polycrystalline Si thin-film solar cells. In spite of the achieved technological progress little is known about the physical properties of the heterojunction interface, in particular about the role of band offsets, the passivation and the effect of interface states.

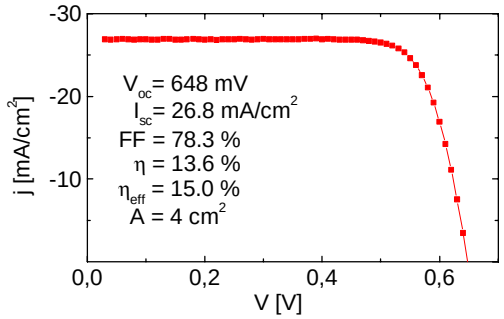

Fig. 1: I-V characteristics of an ITO/a-Si:H(P)/c-Si(p)/BSF heterojunction solar cell under AM1.5 illumination.

A standard preparation procedere was developed for the a-Si/c-Si heterojunction solar cells: The emitter, phosphorus-doped amorphous silicon, a-Si:H(P) about 20 nm thick, was deposited on a p-type Si(111) wafer (350 µm) by standard PECVD at T=210 °C. The c-Si wafers had a back-surface field and were pretreated by a HF-dip (3 % HF:H_2O) prior to the deposition. The front contact was made by a transparent conducting oxide (80 nm of ZnO or ITO) deposited by sputtering. With this standard procedure an efficiency of η=13.6 % was obtained on an area of 4 cm² without adding any additional high-tech feature to cell structure. The good quality of the heterojunction is confirmed by a value of η_{eff}= 15.0 % for the effective area efficiency (Fig.1). The modification of the interface properties by applying various wet- chemical pretreatment procedures led to the result that the lowest interface recombination velocity and the highest efficiency were obtained for the atomically flat and H-terminated Si surface. The electrical and photoelectrical studies of the TCO/a-Si/c-Si structures showed that the optimization of both the interface treatment and the deposition procedure for the a-Si:H(P) film are of crucial importance for the device performance. Since it turned out that the band profile in the c-Si wafer is to some extend determined by the TCO layer the optimization of the emitter must include the entire TCO/a-Si:H/c-Si film structure [1,2].
For a more detailed understanding we have modeled and numerically simulated the device behavior taking into account of the complex electronic structure of a-Si:H(P) and of the c-Si surface. Fig. 2 addresses the question whether there are intrinsic advantages in the use of n- or p-type c-Si wafers by plotting the efficiency as a function of the respective band-offset in the minority carrier bands. Using internal photoemission spectroscopy (IPE) we determined the band offset in the conduction and valence band, ΔE_C for c-Si(p) and ΔE_V for c-Si(n), to about 0.1 eV and 400-500 meV, respectively. If interface states are neglected the efficiencies for a-Si(P)/c-Si(p) and a-Si(B)/c-Si(n) are comparable. However, if interface states are introduced which enhance recombination the efficiency is more strongly reduced for the a-Si(P)/c-Si(p) structure as compared to the opposite configuration. A reasonable explanation for this result is that the higher band offset of the a-Si(B)/c-Si(n) structure causes strong inversion at the interface which results in a considerable reduction of recombination.

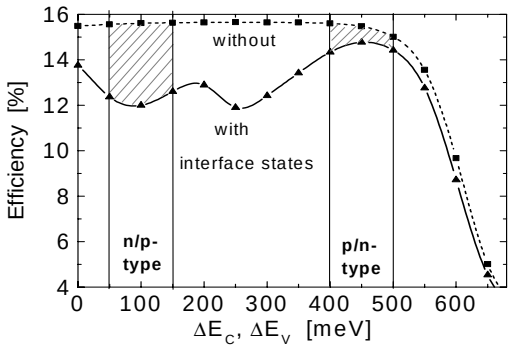

Fig. 2: Influence of the band discontinuity of the minority carrier band of crystalline silicon on the cell efficiency. The ranges of the a-Si:H(P)/c-Si(p) and a-Si:H(B)/c-Si(n) structures are indicated. The two curves have been calculated with D_{it}-values of 0 and 10^{12} $cm^{-2}eV^{-1}$.

References

[1] Schmidt, M.; Froitzheim, A.; Stangl, R.; Elstner, L.; Kliefoth, K.; Fuhs, W.:
Photocurrent Analysis in TCO/a-Si:H/c-Si Solarcell Structures
Proc. of 17th Europ. Photovoltaic Solar Energy Conf. (2001) in press

[2] Stangl, R.; Froitzheim, A.; Elstner, L.; Fuhs, W.:
Amorphous/Crystalline Silicon Heterojunction Solar Cells, a Simulation Study
Proc. of 17th Europ. Photovoltaic Solar Energy Conf. (2001) in press

A. Froitzheim, R. Stangl, H. Angermann, L. Elstner, W. Fuhs, K. Kliefoth, M. Schmidt
(SE1.01b Silicon Heterostructures)

Thin organic layers: a new approach for functionalization of Si surfaces

The recent progress in the development of electronic devices on basis of organic semiconductors has considerably raised the interest in studies which explore the potential of organic materials. It appears particularly attractive to use organic films as buffer layers in heterostructures since the large variety of available compounds is expected to enable a systematic engineering of the junction, for instance by a variation of an external dipole moment on the semiconductor surface.

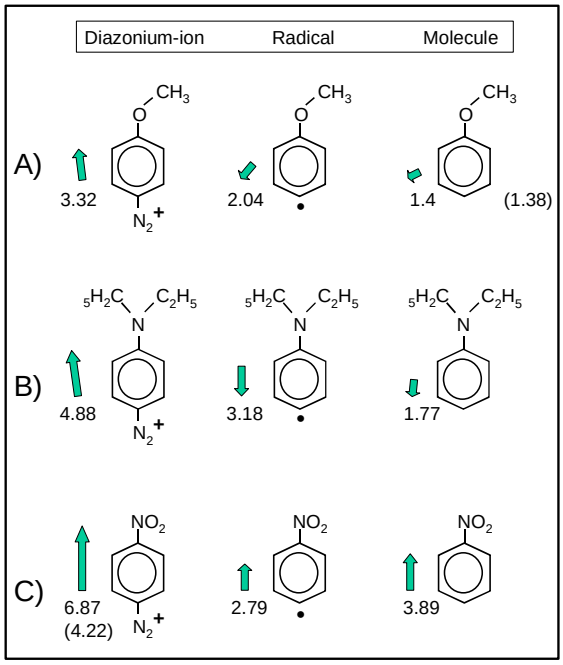

Fig. 1: Changes of the dipole moment and orientation of organic molecules after radical formation during the grafting process as calculated by the DFT method (Dipole strength in units of debye, values in parenthesis are taken from the literature; the orientation is shown by the arrow).

In order to form such organic layers on monocrystalline silicon we used electrochemical grafting of organic molecules on hydrogenated Si surfaces in aqueous electrolytes. The organic molecules consist of a benzene ring with a diazo-group (N_2^+-Ø-G) where G is a variable electron donor or acceptor group which defines the orientation and strength of the dipole moment. Fig. 1 convincingly demonstrates the large variety of available compounds and dipole moments. The deposition process was performed at room temperature by applying a cathodic current to the Si electrode (electron injection into the electrolyte). Cathodic polarization prevents the oxydation of the Si surface. Pulsed in-situ photovoltage (SPV) and an especially designed photoluminescence (PL) techniques, which has been developed in our laboratory, were used to investigate the changes of band bending and of the concentration of active centers for nonradiative recombination. The relative change of the SPV signal by grafting of the organic molecule on the H-terminated Si surface, ΔU_{PV}, is plotted in Fig. 2 as a function of the effective dipole moment perpendicular to the Si(111) surface for various molecules. ΔU_{PV} is a direct measure of the change of the band bending in the c-Si substrate. The grafting of a thin layer of a diazonium compound, diethylaniline or nitrobenzene on atomically flat p-Si(111):H surfaces induces changes of the band bending of about +20 or –110 meV, respectively. The concentration of nonradiative surface defects increases only by a factor of about 3 with respect to the perfect hydrogenated Si surface ($N_s < 10^{11}$ cm^{-2}) which suggests very good passivation of interface states. The changes of band bending are less pronounced when a rough Si surface is used where the dipoles are no longer regularly ordered at the surface [1].

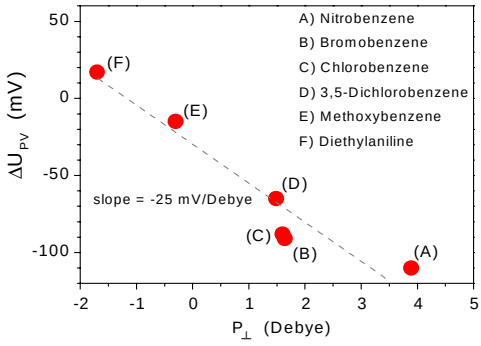

Fig. 2: Change of the photovoltage, ΔU_{PV}, which is directly related to the change in band bending, as a function of the effective dipole moment, p⊥, perpendicular to the Si(111) surface. (A) strongest and (F) weakest electron acceptor group.

These first results are encouraging as they demonstrate good surface passivation and a modification of the electronic structure by thin organic layers. The results show that the band bending in the Si crystal can considerably be modified which possibly is induced by charge transfer via the formed Si-C bonds. A variation in the band offset due to the introduced dipole has still to be shown. The next step will be the formation of electrical contacts on top of these layers in order to study the properties of the films as buffer layers in a device structure.

References

[1] Hartig, P.; Rappich, J.; Dittrich, Th.:
Engineering of Si Surfaces by Electrochemical Grafting of p-Nitrobenzene Molecules
Appl. Phys. Lett 80 (2001) 67-69

J. Rappich, P. Hartig, M. Schmidt
(SE1.01b Silicon Heterostructures)

Department

SE2 Heterogeneous Material Systems

Multi-source evaporation of $Cu(Ga,In)S_2$ for thin-film solar cells

Incorporation of gallium causes a higher absorber band gap. As we have shown in our previous work this leads to a higher open circuit voltage of the solar cell. It was remarkable that the gain in open circuit voltage could be higher than the increase in band gap. The experiments were based on different sequential processes which have in common that metallic precursor films are reacted in a sulfur containing atmosphere. It was found that the reaction kinetics of the sequential processes, via the sequential formation of $CuGaS_2$ and $CuInS_2$, lead to a strong vertical gradient of the [Ga]/[In] ratio in the film. The maximum achievable band gap in the active region of the cell was therefore limited to approximately 1.6 eV, corresponding to a [Ga] / ([In+[Ga]) ratio of 10%. The inherent grading of the gallium content in the active cell region does not allow a full assessment of the electronic influence of Ga. Therefore, we have for the first time used multi-source evaporation to grow $Cu(In,Ga)S_2$ in this reporting period. Four different preparation sequences have been investigated:

- M1: evaporation with constant rates and substrate temperatures,
- M2: evaporation of In,Ga,S at lower substrate temperatures (typically 250 °C) followed by evaporation of Cu,S at higher (typically 500 °C) substrate temperature,
- M3: same as M2 but including a certain amount of Cu (below stoichiometry) already during the first stage,
- M4: same as M3 but with high substrate temperature from the beginning.

Straightforward co-evaporation (M1) resulted in poor reproducibility and unsatisfying material properties. Tentatively, this has been assigned to Cu_xS segregated within the polycrystalline film.

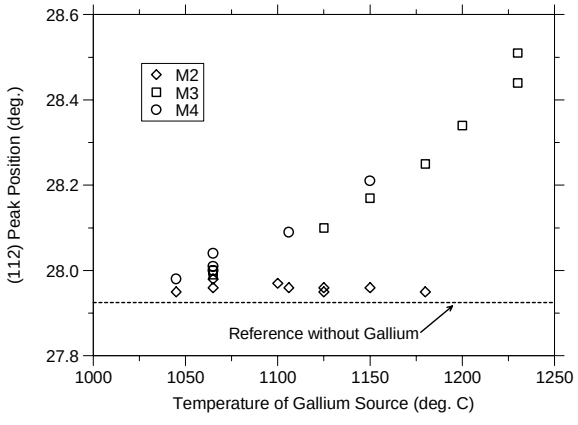

Fig. 1. Position of the (112) reflection in XRD as a function of the gallium source temperature.

The gallium content in the upper part of the film can be judged from its lattice constant. Fig. 1 shows the position of the (112) peak in x-ray diffraction (XRD) as a function of the gallium source temperature. It can be seen that in case of the M2 sequence the lattice constant and hence gallium content of the upper part of the film is almost constant. In general, also taking into account the previous results from sulfurization, there is a certain correlation between the phase formation sequence, the film properties and the homogeneity of Ga distribution.

Sample	E_g eV	V_{oc} mV	j_{sc}* mA/cm^2	ff %	η* %
#94 M2	1.53	776	22.4	74	12.9
#96 M3	1.65	837	18.4	70	10.8
#113 M3	1.74	895	16.2	70	10.1

* Active area

Table 1. Development status of $Cu(In,Ga)S_2$ solar cells (Band gap Eg determined from spectral response).

Re-crystallization, as it must occur in sulfurization and in sequence M2, yields good film properties but as described causes a strong gradient in the Ga distribution perpendicular to the substrate. In M3 and M4, a Cu-poor quaternary chalcopyrite or related compound is already formed during the first stage. This prevents the sequential segregation of $CuGaS_2$ and $CuInS_2$ but also limits the beneficial influence of Cu_xS induced re-crystallization in the second stage. Using sequence M2 we have achieved a new world record for Se-free chalcopyrite solar cells (Table 1, 12.3 % total area efficiency confirmed by the National Renewable Energy Lab, U.S.A.) The more homogeneous Ga profile with M3 and M4 allows higher band gaps, up to values which are suitable for the top cell in a tandem configuration. While the transport properties are clearly inferior compared to the re-crystallized lower band gap material they are still sufficient for more than 10 % efficiency which is a remarkable value at this band gap (Table 1).

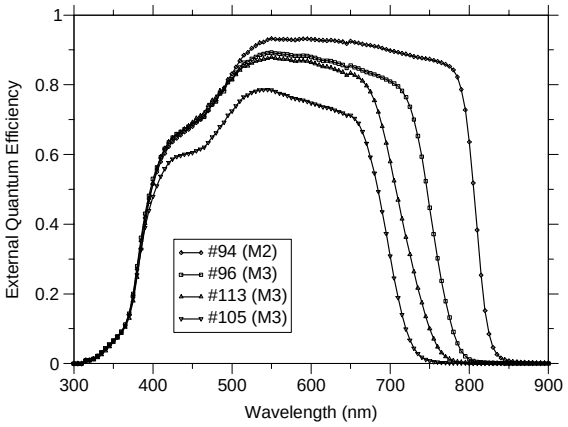

Fig. 2. External quantum efficiency of $Cu(In,Ga)S_2$ solar cells. Homogeneous gallium distribution and hence significantly increased band gap are achieved by using preparation sequence M3.

R. Klenk, R. Kaigawa, C. Kelch, M. Kirsch, A. Neisser, M.Ch. Lux-Steiner
(SE2.05 Chalcopyrite Solar Cells)

(Zn,Mg)O as window layer for Cd-free chalcopyrite solar cells

Current chalcopyrite based thin film solar cells use a complicated three layer window typically consisting of a CdS buffer layer deposited from a chemical bath, an undoped sputtered ZnO layer and a highly doped ZnO:Al or ZnO:Ga layer. The CdS buffer has major drawbacks: it contains Cd and the chemical bath deposition does not integrate well into a production line that is otherwise using only dry vacuum processes. There are indications that the requirement for the undoped ZnO layer is due mostly to technological reasons rather than device physics. Nevertheless, the band line-up at the buffer/ZnO interface could in principle influence the potential drop across the absorber and the Fermi-level position at the absorber/buffer interface. Following a concept proposed by T. Minemoto et al., the band gap of ZnO can be widened by alloying with MgO which should lead to a reduced conduction band cliff. Since band matching is also normally a major task of the buffer layer it might be possible to omit the buffer if an optimized ZnO is used. This would result in a very attractive completely dry cell manufacturing.

We have been able to grow single phase $(Zn_{0.85}Mg_{0.15})O$ films with the expected lattice constant and band gap (Fig. 1) by RF-sputtering from a mixed target. The new TCO has been tested in solar cells based on absorbers with varied band gap between 1.1 and 1.7 eV. The preliminary results can be summarized as follows: substituting the ZnO layer by (Zn,Mg)O has a very small positive influence in cells with a CdS buffer layer for all absorbers. If the CdS buffer is omitted the influence is much more significant. In case of low gap $Cu(In,Ga)(S,Se)_2$ absorbers we have achieved an efficiency of almost 10 % (Fig. 2) which is a remarkable value for completely dry process. With the higher gap absorbers the efficiencies are also increased but still marginal in terms of absolute value.

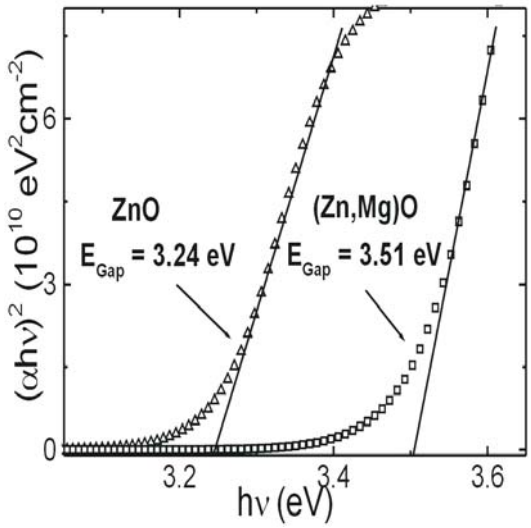

Fig. 1: Determination of the optical band gap of ZnO and (Zn,Mg)O from $(\alpha h\nu)^2$ vs. $h\nu$ plots.

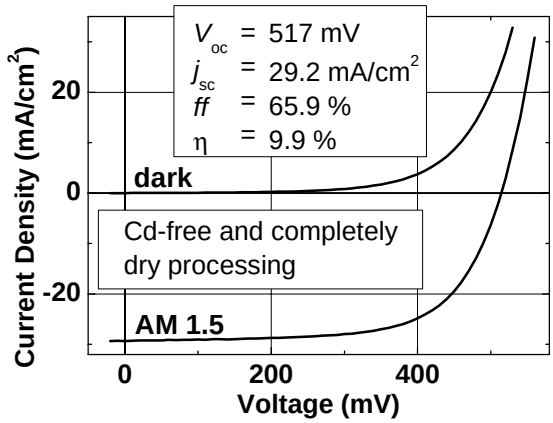

Fig. 2: jV curves of a $Cu(In,Ga)(S,Se)_2$ / (Zn,Mg)O / ZnO solar cell. No wet chemistry was used to prepare this cell.

The expected tendency in band alignment has been confirmed in a model experiment where ZnO, (Zn,Mg)O and ZnO:Ga have been deposited sequentially onto a GaP substrate. A cross section has been prepared by mechanical polishing and investigated in the Kelvin probe force microscope (KPFM) after sputter cleaning (Fig. 3). It is expected that this unique method can assist in developing optimized band alignments throughout the chalcopyrite/buffer/TCO heterostructure.

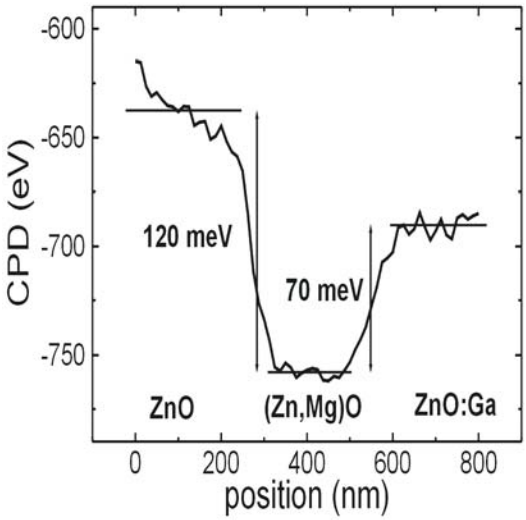

Fig. 3: Contact potential difference CPD as measured by KPFM on the cross section of a polycrystalline film consisting of ZnO, (Zn,Mg)O, and ZnO:Ga deposited sequentially onto a GaP wafer.

Th. Glatzel, R. Klenk, M. Kirsch, S. Sadewasser, M. Ch. Lux-Steiner
(SE2.05 Chalcopyrite Solar Cells)

Analysis of recombination losses in chalcopyrite solar cells

Recombination losses are analyzed by measuring *j(V)* curves as a function of temperature and illumination. The open circuit voltage for state of the art $CuInSe_2$ and $CuGaSe_2$ solar cells from the Ångström Solar Center extrapolates in Fig. 1 for zero Kelvin to values corresponding to the band gap of the considered absorber material, indicating that recombination in the space charge region dominates the current transport. In contrast, this is not the case for our baseline $CuInS_2$ cells. The open circuit voltage extrapolates to values some hundred mV below the value corresponding to the $CuInS_2$ band gap of 1.5 eV, indicating a stronger influence of the $CuInS_2$/CdS interface.

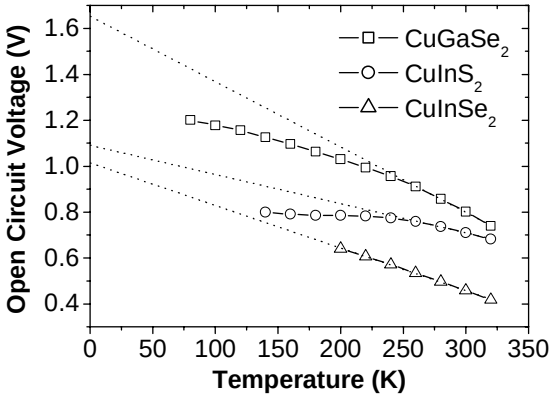

Fig. 1. Open circuit voltage of different chalcopyrite solar cells as a function of temperature

For selenide based cells, different models have been suggested to explain the negligible influence of recombination at the absorber/CdS interface, including a low density of states due to good lattice matching, an n-type ordered vacancy compound (OVC) surface segregation or a buried homojunction by diffusion of Cd into the absorber. We have been able to show, however, that suppression of interface recombination can be a generic feature of any heterojunction if only a few design rules are taken into account. In $CuInS_2$ cells these rules are apparently only partly fulfilled.

The further analysis of the *j(V)* curves in terms of a modified one diode model gives diode quality factors and saturation currents. In contrast to the selenide based cells we learned from the diode quality factors that the dominating recombination mechanism in $CuInS_2$ cells depends on the illumination. For $CuInS_2$ cells in the dark, strongly temperature dependent diode quality factors point to recombination assisted by tunnelling. Under illumination the diode quality factors are significantly lowered, indicating that tunnelling assistance is reduced.

In order to further investigate the illumination induced effects we determine the activation energy of the main recombination in the dark and under illumination, respectively. An Arrhenius plot of the saturation current density with a correction for the temperature dependence of the diode quality factor should yield a straight line where the slope provides the activation energy. For selenide based cells these plots result in activation energies again corresponding to the band gap of the considered absorber material in the dark as well as under illumination. In contrast, we find illumination dependent behavior for $CuInS_2$ cells as shown in Fig. 2. in accordance with our findings from the diode quality factors.

The $CuInS_2$ cells from standard absorber preparations (rapid thermal process RTP) show under illumination activation energies below the band gap, which is believed to be due to recombination at the interface over a barrier which is reduced by the unfavourable band line-up or Fermi-level pinning at the $CuInS_2$/CdS interface. In the dark, the activation energy is at least 0.2 eV higher, with values equivalent to the absorber band gap for cells sulfurized in the conventional thermal process (CTP). These results suggest a change of the dominating recombination mechanism from tunnelling enhanced recombination via traps in the space charge region in the dark to partly tunnelling enhanced recombination via interface states under illumination.

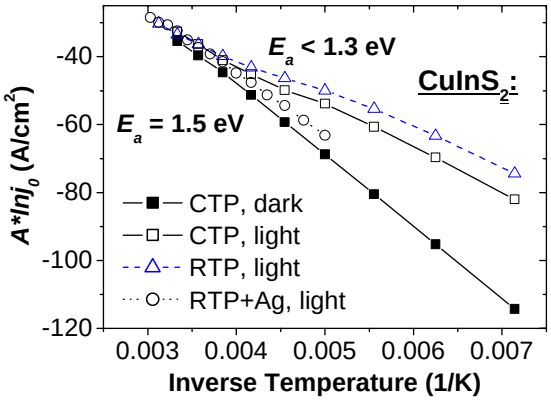

Fig. 2. Corrected saturation currents for $CuInS_2$ cells depending of absorber preparation

As an exception cells where the absorbers were doped with Ag did not exhibit the barrier reduction under illumination. Furthermore, the lateral conductivity of the Ag containing cells is decreased. From these findings we conclude that a reduced net carrier density shifts the dominant recombination away from the interface. Even if this improved open circuit voltages by some 10 mV, the values are still moderate in view of the absorber band gap E_g of 1.5 eV.

J. Reiß, R. Klenk, M.C. Lux-Steiner
(SE2.05 Chalcopyrite Solar Cells)

Transport mechanism of solar cell grade polycrystalline $CuGaSe_2$ thin films

$CuGaSe_2$ as a wide-gap chalcopyrite (Eg=1.68eV) is a promising candidate for high open circuit voltages in solar cells and an ideal partner for copper indium selenide solar cells in tandem photovoltaic devices. However, considerable optimization of $CuGaSe_2$ based solar cells is necessary for this purpose and the limitations of this material in comparison to $CuInSe_2$ are still not clear.
Various studies present transport properties of chalcopyrite single crystals and epitaxial layers but the influence of grain boundaries in device grade polycrystalline material is almost unknown.

Transport studies

In our study the mechanism of charge carrier transport in solar cell grade polycrystalline $CuGaSe_2$ has been studied in the temperature range of 80-350K using Hall effect and conductivity measurements in the dark. Polycrystalline $CuGaSe_2$ layers were grown on soda lime glass substrates by PVD according to our standard process resulting in Mo/$CuGaSe_2$/CdS/ZnO/NiAl solar cells reaching efficiencies of 7.9 % [1]. Figure 1 shows a typical mobility plot of the measured samples.
Mobilities of the polycrystalline films were found to be thermally activated in the temperature range of 150-300K (region II) and are explained by the grain-boundary barrier model developed by Seto [2] for polycrystalline Si assuming thermionic emission of the charge carriers across the grain boundaries. Mobilities are activated according to

$\mu = \mu_0 \exp(E_a / kT)$.

Inter-grain barriers limiting the charge carrier transport and the band bending corresponding to E_a at the grain boundaries were found to vary between 60 and 120meV. Using Poisson's equation a charge density p_t of ~5e11/cm^2 located at the grain boundaries was obtained independent of the doping level i.e. the position of the Fermi-level. Thus a defect state at the grain boundaries above the Fermi-level is concluded.

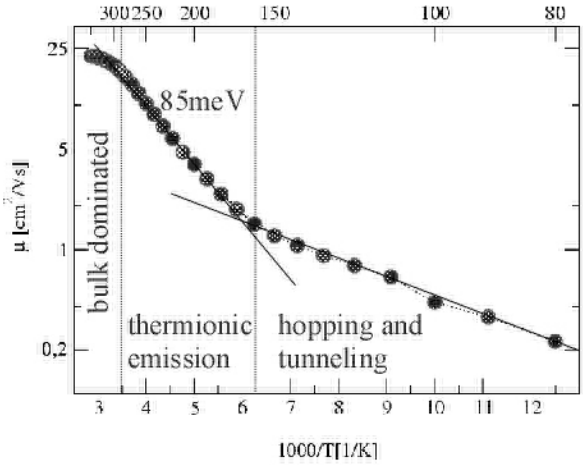

Fig.1: Mobility vs 1/T for typical stoichiometric samples. The regions dominated by different scattering mechanisms are shown.

Above temperatures of 300K (region I) charge transport is not limited by grain boundary scattering, but phonon scattering in the bulk of the grains dominates.
At temperatures below 150K (region III) the activation energy of the mobility lowers indicating a change in the conduction mechanism. Comparison with transport measurements in epitaxial $CuGaSe_2$ films indicates hopping in defect states as the dominating transport path. The resulting grain boundary model is summarized in Fig. 2.

References

[1] S. Schuler, S. Nishiwaki, M. Dziedzina, R.Klenk, S. Siebentritt, M. Ch. Lux-Steiner, Mat. Res. Soc. Symp. Vol.668 (2002) in press

[2] Y. W. Seto, Journal of applied Physics Vol. 46 (75), p.5247

S. Schuler, S. Nishiwaki, N. Rega, S. Brehme, S. Siebentritt, and M.Ch. Lux-Steiner
(SE2.05 Chalcopyrite Solar Cells)

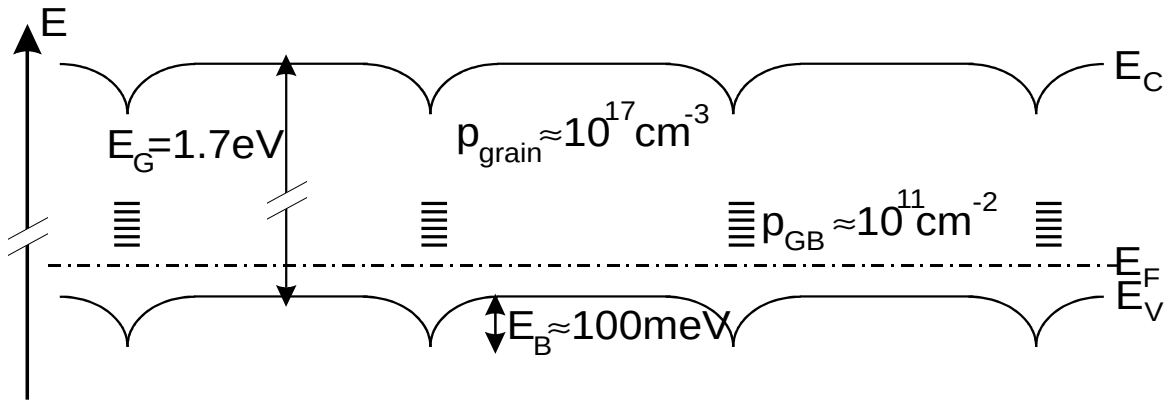

Fig.2: Concluded grain boundary model. E_C, E_V, E_F conduction band, valence band and Fermi-energy-level, E_B grain boundary barrier, E_G band gap, p_{grain} bulk doping density, p_{GB} grain boundary defect density.

$CuGaSe_2$ by Chemical Vapor Deposition (CVD)

Recent improvements of the CVD-process

A stoichiometric volatility and therefore improved material yield of the source material for CGS preparation was achieved by switching from a single $CuGaSe_2$ powder source to two binary sources, Cu_2Se and Ga_2Se_3 [1]. The gas phase composition can be accurately adjusted by modifying the flow of the halide transport agents for Cu_2Se and Ga_2Se_3, HI and HCl respectively. For this set up a two-stage deposition process has been adapted: i) in the first stage nearly stoichiometric CGS is grown during 3-4 hours at a substrate temperature of 500°C and thereafter ii) just Ga_2Se_3 is transported for 20 min to the sample side at 530°C. The first stage provides high-quality crystallites with grain sizes in the range of 1.5 µm. The second stage ensures a final overall slightly Ga-rich composition for optimal device performance.

Photoluminescence of CVD grown $CuGaSe_2$

Different from other deposition methods, the photoluminescence (PL) of CVD grown $CuGaSe_2$ thin films exhibit a deep luminescence peak located around 1.3 eV. This CVD-specific radiative recombination mechanism has been related with a deep acceptor-like defect band around 240 meV, probably caused by V_{Ga} [2]. Chemical calculations assisted with ChemSage software revealed the active role Ga plays in the removal of iodine species from the saturated sample-side atmosphere in the CVD reactor. The thus reduced amount of Ga available for incorporation into the solid film, together with the high growth rate would favor the formation of V_{Ga}. After the second stage leading to an overall Ga-rich composition a significant decrease of the 1.3 eV signal is observed (Fig.1).

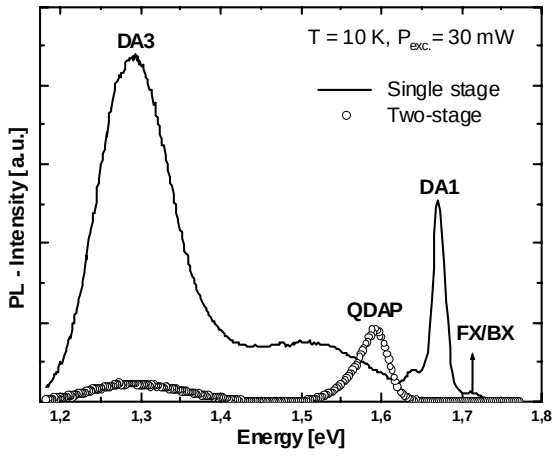

Fig. 1: PL spectra of samples after completion of the first stage (solid line) and after the second stage (dotted). Notation of peaks follows [2].

Device performance

We have recorded a relative improvement of more than 20 % in the efficiency of two-stage grown samples compared to previous cells based on slightly Ga-rich single-stage CGS absorbers (see Table 1).

Sample	Voc (mV)	Jsc (mA/cm2)	FF	Eff (%)
Single-stage	684	11.7	0.51	4.1
Two-stage	804	12.9	0.57	5.9

Table 1: Comparison of PV parameters under AM1.5 illumination of cells grown by single- and two-stage processes, used for the analysis.

The highest efficiency value achieved so far is 6.1% (V_{OC} up to 844 mV) under AM 1.5 illumination Quantum efficiency as well as EBIC (electron beam induced current) measurements reveal an enlarged space charge region for the two-stage processed samples (Fig.2) [3]. This result can be explained by the lower doping level of Ga-rich material due two a higher degree of compensation. In accordance with the enlarged space charge region of two-stage based devices the tunneling contribution to the electronic transport is reduced, identified from the diode ideality factor in current voltage analyses, leading to a better device performance.

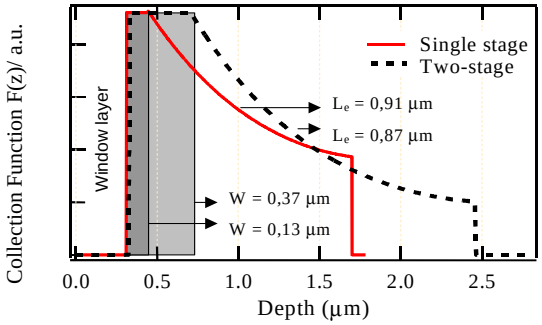

Fig. 2: Collection function profile from EBIC data of single-stage (solid) and two-stage (dotted) samples. The SCR (shaded) is enlarged after the second stage (from 0.13 to 0.37 µm) and the minority carrier diffusion length slightly reduced (from 0.91 to 0.87 µm), compared with single stage sample values.

Microstructure of ZnO/CdS/$CuGaSe_2$/Mo Interfaces

Actual chalcopyrite based solar cells are characterized by a complex polycrystalline structure. Microstructural characterization by transmission electron microscopy (TEM) and scanning probe microscopes assists in refinement of the device models when correlated with electrical measurements.
The microstructural properties of the different interfacial regions have been studied in the CVD-ZnO/CdS/$CuGaSe_2$/Mo solar cell heterostructure in cooperation with SF/BENSC and the Fritz-Haber-Institute of the MPG. The $CuGaSe_2$-film was prepared by the two-stage-process. High-resolution transmission electron microscopy (HRTEM) combined with scanning energy dispersive X-ray detection (EDX) shows the formation of an interfacial

$MoSe_2$-layer (Fig. 3) at the back contact, while, on the other hand, no Cu-Se precipitates have been found neither at the CdS/$CuGaSe_2$-interface nor in the grains of the absorber film, as usually detected in Cu-rich $CuGaSe_2$-thin film solar cells [4].

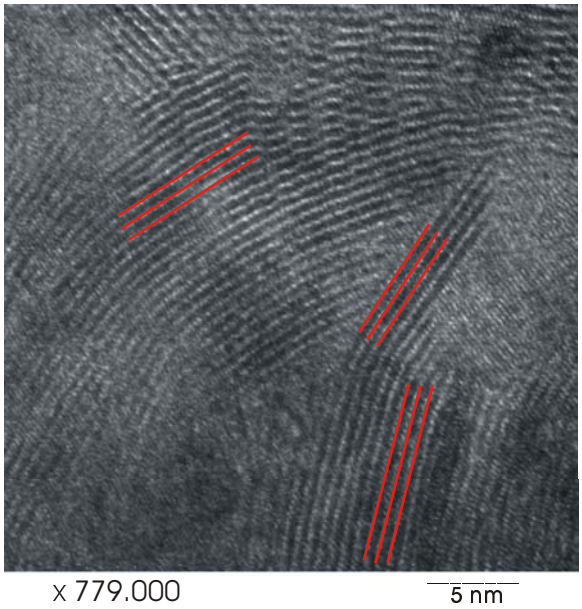

Fig. 3: High-resolution TEM picture of the interfacial $MoSe_2$ film found in the ZnO/CdS/$CuGaSe_2$/Mo solar cell heterostructure.

Thin interfacial $MoSe_2$ films have thickness of ~150 nm and are formed only onto soda-lime glass substrates. This suggests a promoting behavior of the diffusing Na cations in the formation process of the layered structure of $MoSe_2$ onto the metallic Mo film. The $MoSe_2$ layers are stacked together by weak Van-der-Waals forces and, as shown in Fig.3, these layers have a distance of ~6.5 Å in very good agreement with the literature, and are oriented almost perpendicular or tilted to the Mo-back contact plane (i.e. the c-axis of the hexagonal lattice is almost parallel or tilted to the substrate plane).
Kelvin probe force microscopy (KPFM) investigations on the cross-sectional ZnO/CdS/$CuGaSe_2$/Mo heterostructure are shown in Fig. 4 and reveal clear variations of the work function indicating well defined electronic transitions at the interfaces. This is important since a second junction at the back contact of the solar cell would severely reduce the maximum solar-to-electric conversion efficiency. TEM and KPFM reveal that process conditions in the CVD favor the formation of a $MoSe_2$ layer between back contact and absorber. This can be correlated with a roll-over of the jV(T) characteristics at low temperatures (blocking diode) as shown in Fig. 5.

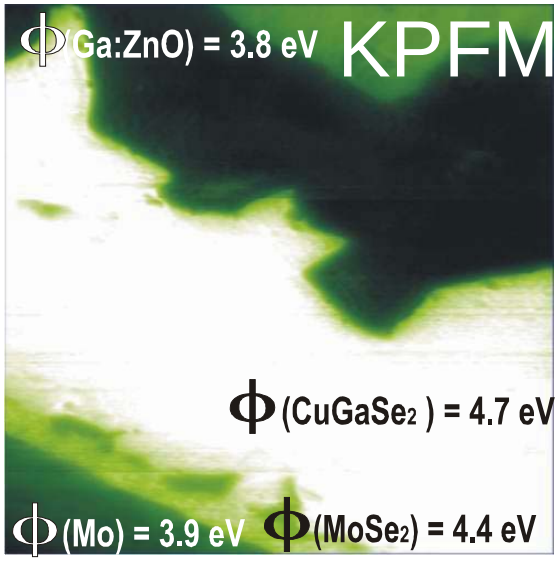

Fig. 4: Kelvin probe force microscopic picture of the ZnO/CdS/ $CuGaSe_2$/Mo solar cell heterostructure.

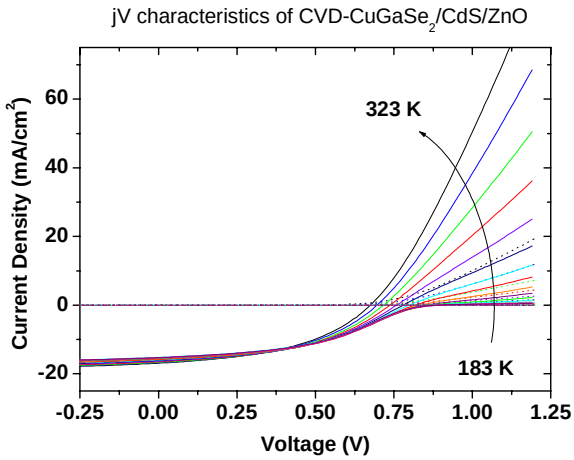

Fig. 5: Temperature-dependent jV-characteristics of the ZnO/CdS/ $CuGaSe_2$/Mo solar cell heterostructure.

References
[1] D. Fischer et al., Solar Energy Mat. Solar Cells 67 (2001) 105.
[2] A. Meeder et al., Thin Solid Films, 403-404 (2002), 495-499.
[3] D. Fuertes Marrón, et al., Proc. 17th Int. PVSEC Conf. Munich.
[4] see, for example: V. Nadenau et al., Journal of Applied Physics 85 (1999) 534.

S.M. Babu, D. Fuertes Marrón, Th. Glatzel, K. Höhn, A. Jäger-Waldau, A. Meeder, T. Münchenberg, A. Rumberg, M. Rusu, Th. Schedel-Niedrig, S. Wiesner, R. Würz, M. Ch. Lux-Steiner (SE2.05 Chalcopyrite Solar Cells) in collaboration with N. Pfänder, H. Sauer (Fritz-Haber-Institute), P. Schubert-Bischoff (SF/BENSC)

Interdiffusion study at the ZnSe / Cu(In,Ga)(S,Se)$_2$ heterojunction by ERDA measurements

A co-operation of the CSVT group and the ERDA group of the ISL is engaged in investigating diffusion processes at the ZnSe / Cu(In,Ga)(S,Se)$_2$ heterosystems. The aim of the project is the quantitative determination of interdiffusion processes of chemical elements at the heterojunction. As previously shown the ZnSe deposition on chalcopyrite absorbers using chemical vapor deposition (CVD) or metal organic CVD (MOCVD) needs a minimal deposition temperature of 280 °C / 265 °C due to reaction kinetics in the gas phase. Additionally, the homogeneity of the coverage and the layer quality increase with increasing temperature. Therefore, one would expect higher solar cell efficiencies with enhanced deposition temperatures. In contrast to this, best results were found for the lowest temperatures and shortest deposition times. The question arises if structural changes may occur during the deposition. Thus, the structural composition of the layers is investigated by means of heavy ion elastic recoil detection analysis (HI-ERDA). From the amount of the scattered atoms detected, the ejectiles, this technique allows to determine the absolute concentration of all chemical elements of the sample simultaneously. Furthermore, the depth distribution of the element concentration can be calculated from the energy of the ejectiles.

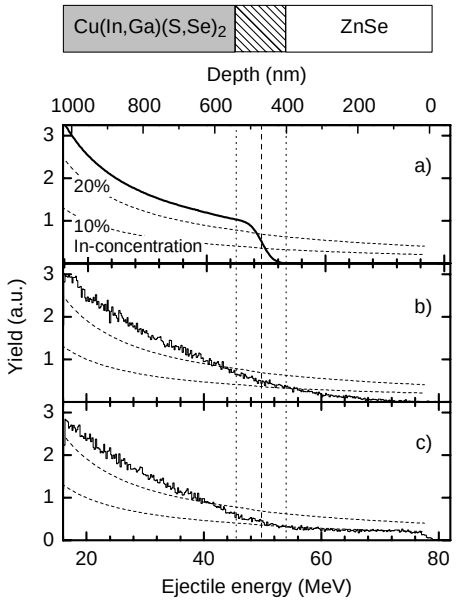

Fig. 1: Qualitative demonstration of In diffusion from the polycrystalline Cu(In,Ga)(S,Se)$_2$ absorber into the ZnSe buffer measured with 143 MeV ^{86}Kr projectiles at a scattering angle of 40 °. (a) Simulation of the In energy spectrum taking into account surface and interface roughness as derived from AFM and the corresponding sulfur spectrum without diffusion. (b) Measured In spectrum of an as grown sample. (c) Measured In spectrum of a sample after annealing for 5h at 400 °C.

Fig. 1 shows an example of In profiles from ZnSe / Cu(In,Ga)(S,Se)$_2$ heterostructures grown by CVD at 350 °C for 3h. Fig. 1a depicts the spectrum as it was expected theoretically without In-diffusion. Fig. 1b and fig. 1c show the measured In spectra of an as grown sample and of a sample which was annealed at 400 °C for 5h, respectively. The occurring of In-ejectiles with energies above 50 MeV indicate the presence of In atoms in the depth region of the ZnSe buffer layer. For the case after annealing the fraction of In is significantly enhanced up to 80 MeV, corresponding to the surface of the samples. This proves the diffusion of the In from the absorber into the buffer layer qualitatively.

For the quantitative discussion of diffusion parameters, it is necessary to understand the effect of surface roughness. As the beam spot has a finite area (some mm^2), roughness results in a distribution of path lengths for the individual projectile/ejectile couples and, therefore, in a broadening of the energy spectra. If this effect is unfolded, the remaining energy broadening corresponds to diffusion.

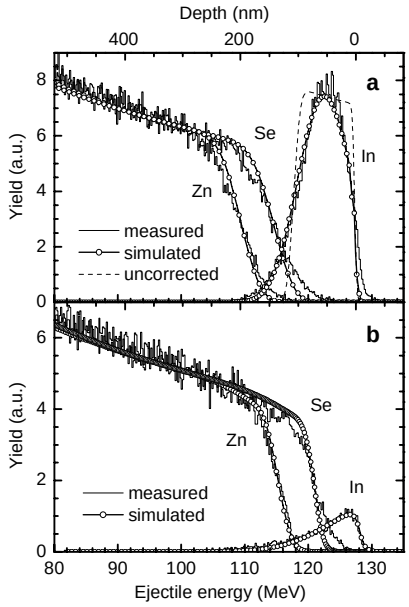

Fig.2: Experimental and simulated spectra obtained from a ZnSe single crystal covered with a 90nm thick In layer, including roughness corrections. The measurements were performed with a 230 MeV ^{129}Xe beam. (a) As grown sample. A mean roughness of ±45nm has been determined by means of AFM. The dashed curve represents the simulation calculation for In without roughness correction. (b) The result for a second part of the sample analyzed after annealing for 5h at 350 °C

S. Lindner (SE2.05 Chalcopyrite Solar Cells) in collaboration with W. Bohne, J. Röhrich, E. Strub (SF4)

Kelvin probe force microscopy

Kelvin probe force microscopy (KPFM) in ultra-high vacuum allows to simultaneously obtain structural as well as electronic information (work function Φ) of a sample's surface with an extremely high lateral (~ 20 nm) and energy resolution (~ 5 meV).
The application of the KPFM to a solar cell absorber material was demonstrated using $CuGaSe_2$ deposited on Mo covered glass by chemical vapor deposition. Figure 1 shows the topography (b) and the work function (a) of the $CuGaSe_2$ film in dark conditions. The work function of the illuminated (20 mW, 675 nm) sample is shown in Fig. 1 (c). In the topography the granular structure of the polycrystalline film is clearly visible. Except for one grain (indicated by the ellipse) at the bottom of the image the work function increases homogeneously under illumination. This becomes clearer in Fig. 1 (d) where a line scan through the images is presented. The major part of the sample shows an 80 meV increase under illumination with only one grain showing a 200 meV decrease, which was attributed to a $CuSe_x$ impurity phase.

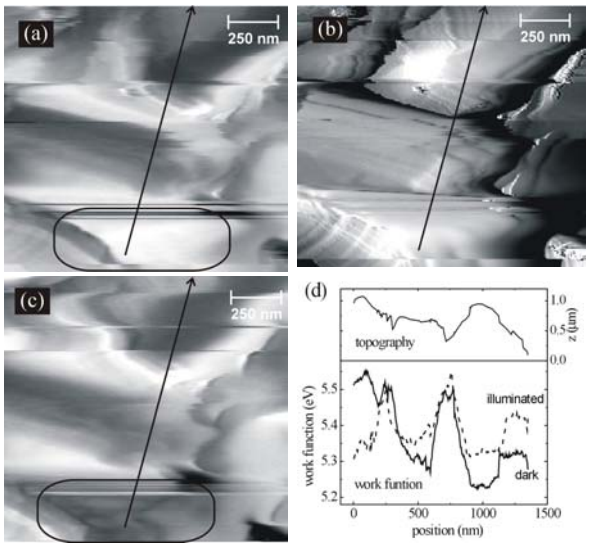

Fig. 1: KPFM measurements of $CuGaSe_2$ on Mo/glass. ***(a)*** *work function image (Φ = 5.14 eV – 5.53 eV) of the surface in the dark,* ***(b)*** *simultaneously measured topography image (gray scale ≈ 1044 nm),* ***(c)*** *work function image of the surface under illumination with 20 mW at 675 nm (Φ = 5.21 eV – 5.53 eV),* ***(d)*** *line scans of the topography and work function.*

The surface of a MOVPE-grown $CuGaSe_2$ film on a ZnSe (110) single crystalline substrate is shown in Figure 2. Again the topography (a) shows the grains of the polycrystalline film. However, x-ray diffraction revealed a film orientation along the (220) direction of the $CuGaSe_2$ unit cell. The corresponding work function image in Fig. 2 (b) clearly shows different areas of constant work function, which coincide with the crystal facets of the grains observed in the topography. In Fig. 2 (c) this is demonstrated more clearly: the topography is represented as the 3D effect and the work function is superimposed on this image represented by the color scale. The observed work function difference in dependence of the orientation of the crystal facets is due to a surface dipole which is characteristic for each orientation. For this oriented film, an analysis of the angles between the facets allows to determine the surface orientation of the facets, as indexed in Fig. 2(b). The observation of such a wide variation (up to 250 meV) of Φ within one surface will influence the band alignment to a subsequently built-up heterostructure and might have a detrimental effect on the solar cell efficiency.

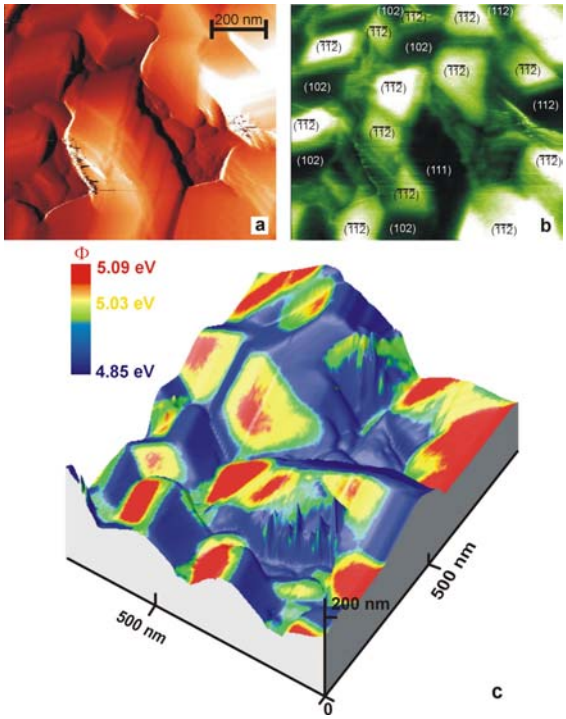

Fig. 2: KPFM measurement of a $CuGaSe_2$ thin film grown on ZnSe(110) by MOVPE. ***(a)*** *The topography image shows distinct crystal facets on the (220) oriented $CuGaSe_2$ film. The colour scale corresponds to height differences of 384 nm.* ***(b)*** *Representation of the simultaneously measured work function (Φ = 4.85 ... 5.09 eV). The crystallographic orientation of the facets is indicated.* ***(c)*** *3-dimensional image merging the topography (as the 3D effect) and the work function represented by the color scale. The origin corresponds to the lower left corner in the 2D images.*

S. Sadewasser, Th. Glatzel, M.Ch. Lux-Steiner (SE2.05 Chalcopyrite Solar Cells)

Chemical and electrochemical deposition of chalcogenides for solar cells

Presently, interest for deposition of chalcogenide semiconductors from solution emerged as competitive techniques for the fabrication of thin films for solar energy conversion. Among the various solution growth methods, chemical bath deposition (CBD) and electrodeposition (ED) techniques can offer convenient, low cost and environmentally compatible tools. The CBD process does not involve electron exchange with a conducting substrate and appears to be the best technique for depositing buffer layers in high efficiency large area thin film chalcogenide devices.

ZnS and ZnSe by CBD

ZnSe and ZnS buffer layers are deposited on $Cu(In,Ga)(S,Se)_2$ (CIGSS) substrate using an aqueous alkaline solution using a solution (A) which consists of metallic cation precursor $ZnSO_4$ and two different ligands NH_2NH_2 (25%), NH_3 (25%) dissolved in tri-distilled water under stirring and heated to the appropriate temperature and the chalcogene source (solution B) containing either $SeC(NH_2)_2$ and Na_2SO_3 or its sulfur analogue $SC(NH_2)_2$ dissolved in tri-distilled water.The CBD consists of a heterogeneous process, where ZnX (X = S, Se) and $Zn(OH)_2$ grows on the substrate surface and a homogenous one which consists of the precipitate of ZnX and $Zn(OH)_2$. We investigated by using HRTEM of the CBD-precipitate after ZnSe deposition. We observed the precipitation of ZnSe nanocrystallites as agglomerates in a cluster structure (see inset in Fig. 1). Fourier analysis yields a lattice plane spacing of d = 3.2 nm. It can be attributed to hexagonal ZnSe [002] and/or cubic ZnSe [111]. Previous results showed that nanoclusters of the same orientation and size could be found in the buffer layer deposited on CIGSS substrate. Since crystallites of the same spacing and dimension are found in buffer layers, we believed that ZnSe precipitates (homogeneous reaction) stick to the surface of the absorber. The mechanism of growth is by colloid aggregation.

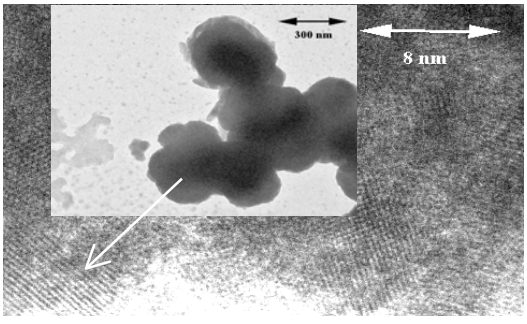

Fig. 1: Remains of the CBD-solution on a Cu grid as revealed by TEM (inset) and HRTEM.

The reactions commonly accepted are:

$$XC(NH_2)_2 + 2OH^- \Rightarrow X^{2-} + CN_2H_2 + 2H_2O$$

$(Zn^{2+})L_n \Rightarrow Zn^{2+} + nL$ and $Zn^{2+} + X^{2-} \Rightarrow ZnX$ The global reaction is:

$Zn(NH_3)_4^{2+} + XC(NH_2)_2 + 2OH^- \Rightarrow ZnX + 4NH_3 + H_2O$

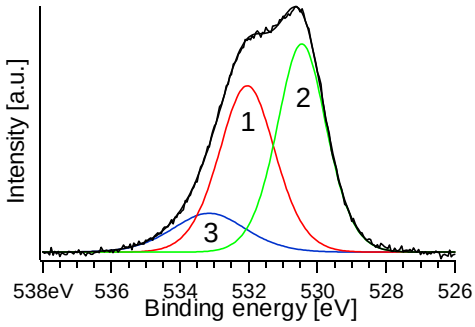

Fig. 2: O_{1s} -XPS spectrum of a CBD-ZnSe on CIGSSe showing ZnO, $Zn(OH)_2$ and C-O.

The ZnSe (or ZnS) film grows with slow release of Se (or S) mainly due to hydrolysis of $SeC(NH_2)_2$ (or $SC(NH_2)_2$) in basic solution. Zn^{2+} ions are released by the decomplexation of $(Zn^{2+})L_n$, where L is the ligand species. When the ionic product of Zn^{2+} and X^{2-} exceeds the solubility product of ZnX, the precipitation of ZnX occurs either in the solution or at surface of the absorber. The formation of ZnSe colloids occurs first in the solution as supported by TEM investigation (Fig. 1). However the hydrolysis of $SC(NH_2)_2$ is rather slow and the formation of ZnS at the surface of the substrates via a heterogeneous process is possible.

The presence of $Zn(OH)_2$ in the deposit is unavoidable due to the aqueous nature of the bath. XPS analysis (Fig. 2) revealed that a large amount of oxygen was included in the CBD-ZnSe film in the form of $Zn(OH)_2$ and H_2O.

The peak located at 531.6 eV – 532 eV is attributed to OH^--groups. the peak at 530.5 eV correspond to O^{2-}compounds and the one at 533.1 eV to water and/or C-O bonds.

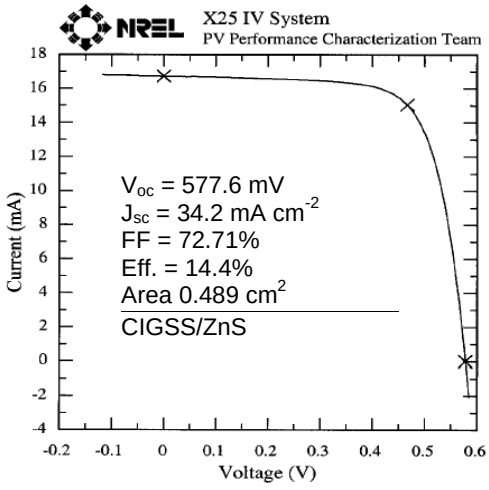

Fig. 3: I-V characteristic of CBD-ZnS/CIGSS solar cell without AR coating.

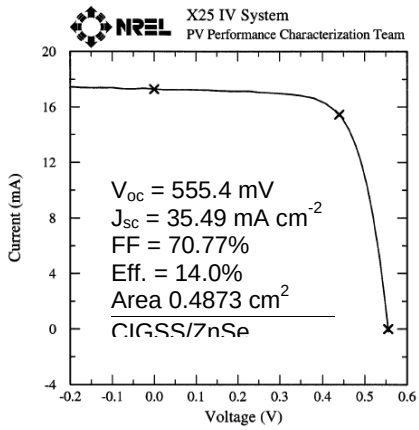

Fig. 4: I-V characteristic CBD-ZnSe/CIGSS solar cell with MgF_2-AR coating

Cell performance

Various photovoltaic devices were fabricated using production scale CIGSS absorber provided by Siemens-Shell. The CBD is a soft process and the CBD-film covers the rough CIGSS surface with a minimum thickness and a high quality pn junction can be formed. Fig. 3 and Fig. 4 show the I-V characteristics of solar cells fabricated using CBD-ZnS and CBD- ZnSe, respectively.
All output characteristics mentioned above were measured by NREL, (Colorado, USA). The devices are submitted to light soaking for 10 minute at P_{max}. under AM1.5, 1000 $W.m^{-2}$ illumination.

Electrodeposition of Cu-In-Ga-Se system

The challenge in this work is to improve the properties of the films prepared already from the electrodeposition step in such a way that they can be used with no or minimal post-treatment.
In order to look for the deposition potential, which will favor the alloy formation, we studied the steady state polarization characteristics of the bath containing $CuCl_2$, $GaCl_3$, H_2SeO_3 and $InCl_3$. Three plateaux are observed at -0,35 to -0,4 V, -0,5 to -0,8 V and -0,9 to -1.2 V corresponding to $Cu_{2-x}Se_2$, $CuInSe_2$ and $CuGa_xIn_{1-x}Se_2$ phases, respectively (see Fig. 5). Above -1.0 V, the current density increases rapidly due to hydrogen evolution. Films deposited at -0.6 V, show the ternary $CuInSe_2$ phase. At -0.9 V, and -1.0 V the film exhibit $CuGa_{0.3}In_{0.7}Se_2$, and $CuGa_{0.5}In_{0.5}Se_2$ phases, respectively.

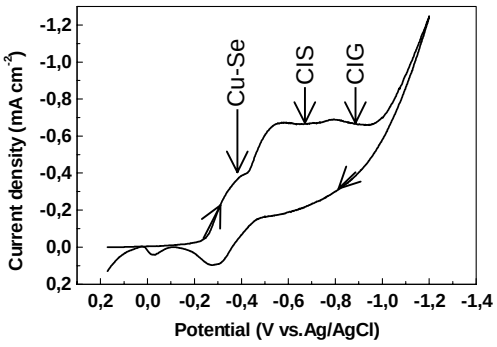

Fig. 5: Cyclic voltammetry on titanium substrate in solution 3mM $CuCl_2$, 50mM $GaCl_3$, 4mM $InCl_3$ and 2mM H_2SeO_3 at pH 2.2.

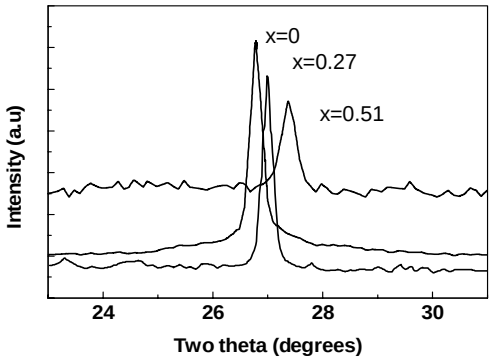

Fig. 6: Bragg peaks (112) positions. The x values represent the Ga content.

All phases are clearly identified by XRD. They show (112), (220, 204), and (116, 312) reflections of the tetragonal structure. Furthermore, we observed a shift of the (112) peaks to larger angles (see Fig. 6). No binary phases such as Cu_xSe and In_2Se_3 are found. Table I gives EDX composition and lattice parameters for as-deposited films grown at various potentials. The composition analysis reveals that the films deposited at potentials -0.6 V, -0.9 V, and -1.0 V on titanium substrates are Se-rich. Diffraction peaks (XRD) from elemental Se cannot be observed in the as-deposited films. This indicates that excess Se in these films is of amorphous phase.

Final Remarks

- ED and CBD are simple and fast, and they can be used for the preparation of binary, ternary and quaternary compounds for subsequent processing into high-quality CIGS thin film absorbers and high efficiency CIGS/ZnX based devices.
- Cd-free devices using production scale absorber are demonstrated and our ZnS and ZnSe buffer layers show efficiencies over 14 % certified at NREL.
- As an initial step, in developing low cost and Cd-free thin film solar cells, it was demonstrated that device quality of single phases $CuGa_xIn_{1-x}Se_2$ can be prepared by electrochemical method at low temperature. The composition is controllable by applied cathode potential and by concentration of elements in the electrolyte.

Table 1: EDX composition and lattice parameters for films electrodeposited at various potentials

E (V vs.Ag/AgCl)		-0.6	-0.9	-1.0
EDX Comopsition (at.%)	Cu	26.36	25.91	22.18
	Ga	0	6.12	12.47
	In	21.35	16.1	11.92
	Se	52.29	51.87	53.43
x = [Ga]/[Ga]+[In]		0	0.27	0.51
Lattice const.				
	a (Å)	5.77	5.73	5.64
	c (Å)	11.68	11.47	11.34
Phase present		$CuInSe_2$	$CuGa_{0.3}In_{0.7}Se_2$	$CuGa_{0.5}In_{0.5}Se_2$

A. Ennaoui, W. Eisele, M.C. Lux-Steiner (SE2.06 New Materials)

Buffer layers, alternative sequential thin layer technology (ILGAR)

The project comprises the development of sequential chemical methods for the deposition of semiconductor thin layers. In the center of interest stands the versatile and robust ILGAR process (Ion Layer Gas Reaction, patents by HMI) featuring low-cost equipment, economical material consumption and low temperature as well as easy controllability of chemical composition, layer thickness and electronic and optical properties.

The ILGAR Process

ILGAR is a sequential and cyclic process which can be fully automated and easily up-scaled. It consists basically of the following steps:

1. Application of a precursor solution on a substrate by dipping or spraying.
2. Reaction of the dry solid precursor layer with a hydrogen chalcogenide gas.

→ Repetition of this process cycle, until the desired layer thickness is obtained.

Sulfide layers are deposited by converting a metal salt by H_2S as reactant gas. Here, selected results from ILGAR oxide layers are presented. A substantial process modification opened the access to these technologically extremely interesting films. A H_2O/NH_3 gas mixture converts the precursor salt to the corresponding hydroxide which undergoes dehydration to the oxide when moderately heated. However, thermodynamic calculations of the system $ZnCl_2$ / H_2O / NH_3 revealed ZnO as the only stable Zn compound under ILGAR conditions even at room temperature (co-operation with Dr. Fiechter, HMI). In spite of this, UV-spectroscopic findings and the absence of any X-ray diffraction signal (XRD) pointed to the formation of meta stable amorphous $Zn(OH)_2$ films at 25°C. Finally, we succeeded in confirming this identity by FTIR reflection spectroscopy (in co-operation with the IWS Dresden, B. Leupolt). Fig. 1 shows the FTIR spectra of ILGAR ZnO layers deposited at various process temperatures: (i) at room temperature, (ii) at 155°C (the typical temperature for window extension layers (WEL) in $Cu(InGa)(S,Se)_2$ („CIGSSe“) solar cells, vide infra) and (iii) at 155°C with an additional annealing at 300°C to ensure complete dehydration. The spectra of bare substrate and a rf-sputtered ZnO sample are given for comparison. The presence or absence of the OH-stretching vibration and the shift in the ZnO-stretching vibration allows a distinction between zinc hydroxide and oxide.

The Window Extension Layer Concept (WEL)

We developed the novel WEL concept for buffer layers. WELs consist of the same material as the sputtered window, but deposited by a mild process. CIGSSe based solar cells with an ILGAR ZnO WEL reached significantly higher efficiencies than the reference cells with the standard CdS buffer (Fig.2). Here the classical cell structure with a sputtered window bilayer consisting of i- ZnO and ZnO:Ga was applied. Even more promising is a novel cell structure with WEL and only the sputtered doped window layer (ZnO:Ga), i.e. one complete sputter step (i-ZnO) can be omitted. This is especially advantageous for the production of solar modules where the substrates have to be removed from the sputter chamber for the scribing in-between the two sputter processes. The cell performance is already comparable with the standard structure (Fig. 2).

With ZnO WELs already a large number of cells has been produced showing statistics and reproducibility. Standard cell concept with sputtered i-ZnO layer: The average efficiency of 80 cells (the 6 best cells out of 8 on each device taken from a series of ten devices) is η_{80}= 13.6 % though the series still contains some process optimization. For the innovative cell concept with ZnO WEL but without *sputtered* i-ZnO layer η_{80}= 13.8 % was achieved. A first up-scaling experiment resulted in a 5x5 cm^2 mini-module with an efficiency η=10.9 %.

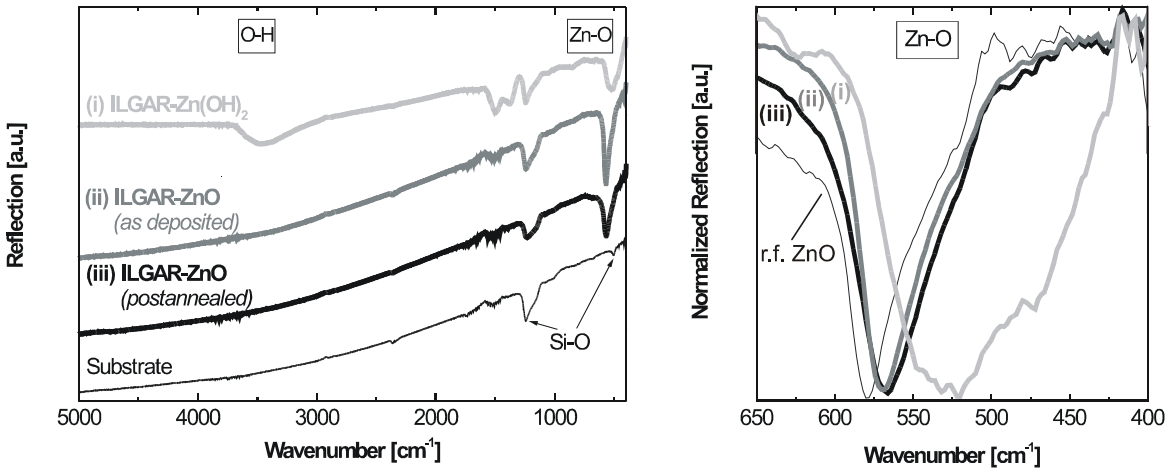

Fig. 1: Left: FTIR reflection spectra (75°/p-polarization) of ILGAR-$Zn(OH)_2$ and ZnO layers, respectively, prepared under different process conditions as described in the text. Right: expended region of the Zn-O-stretching vibration, for comparison the band of a rf-sputtered ZnO sample is shown.

	ILGAR ZnO WEL	Ref. CBD CdS	ILGAR ZnO WEL	Ref. CBD CdS
V_{OC} [mV]	**587**	589	581	**597**
J_{SC} [mA/cm^2]	**35**	33	35	**34**
FF [%]	**72**	73	71	**72**
η [%]	**14.6**	14.1	14.5	**14.7**

Fig. 2: Solar cells with ILGAR ZnO WEL with and without sputtered i-ZnO window layer (CIGSSe absorbers from Siemens&Shell Solar GmbH (SSSG), reference with CBD-CdS buffer)

Absorber Pretreatments

CIGSSe solar cells with ILGAR ZnO WEL reach excellent efficiencies only after a "partial electrolyte" pre-treatment of the absorber similar to that of Ramanathan (i.e., a warm aqueous $CdSO_4$ or $ZnCl_2$/ammonia solution). The nature of surface modifications induced by these treatments is still under debate. In order to gain more insight the absorber surface was investigated by photoelectron spectroscopy after various procedures in a close cooperation with the University of Würzburg (L. Weinhardt, Dr. C. Heske, and Prof. E. Umbach).
First, pure aqueous KCN (3 min, room temperature) or ammonia solutions (10 min, 80°C) were applied to CIGSSe absorbers from Siemens Solar Industries (USA). Both treatments lead to a removal of Na and a strong reduction of oxides. As an example, Fig. 3a shows the complete removal of SeO_2. Moreover, a reduction of In and Cu oxides can be identified. The treatment with NH_3 also leads to a partial removal of the surface C content. In contrast, Fig. 3b shows an increase of the C signal after the KCN treatment, and, furthermore, a deposition of K on the absorber surface. Finally, we observe a strong increase in the S content at the surface after both treatments and, in the case of KCN, a decrease of Cu.
In a second experiment SSSG absorbers were treated with an aqueous NH_3 solution containing $CdSO_4$ or $ZnCl_2$. The survey spectra after both treatments are shown in Fig. 4 in comparison with the spectrum of an untreated absorber. Possible compounds that are compatible with the Cd 3d and Cd MNN line positions are CdS and CdSe, while the Zn-treatment leads to a deposition of $Zn(OH)_2$. To gain further insight into the Cd-treatment process a series of absorbers treated with different $CdSO_4$ concentrations were investigated. We find that the highest $CdSO_4$ concentrations lead to an enhanced Cd deposition and an increase of the oxygen signal. Simultaneously, we observe a shift of the Cd MNN Auger line to lower kinetic energies. The resulting compound can be identified as $Cd(OH)_2$.

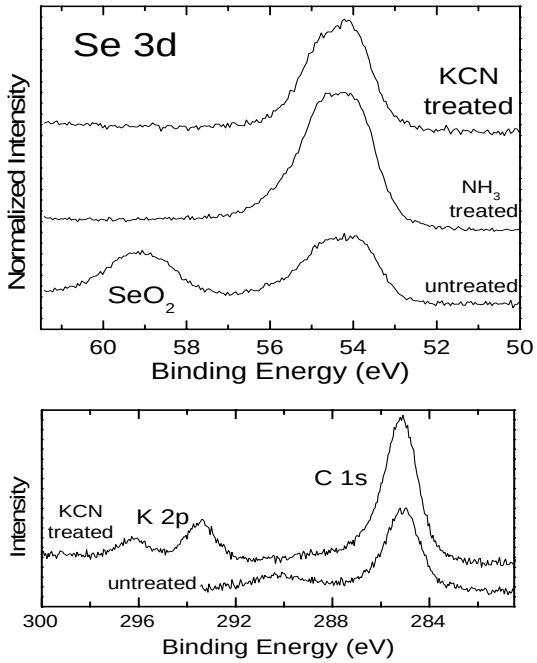

Fig. 3: XPS spectra of CIGSSe absorber surfaces before and after a 10 min treatment with aqueous KCN or ammonia at 80°C, Se 3d (top) C 1s / K 2p (bottom).

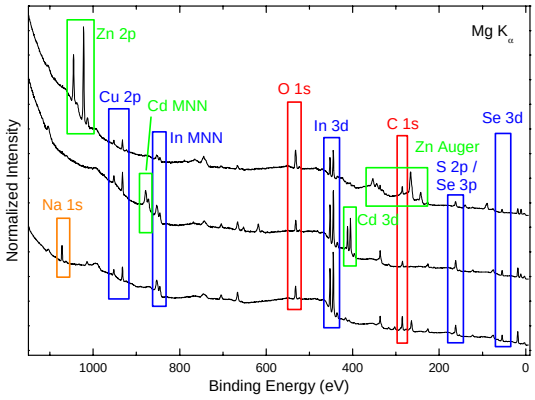

Fig. 4: XPS survey spectra of CIGSSe absorbers before (bottom) and after treatments with aqueous $CdSO_4/NH_3$ (center) or $ZnCl_2/NH_3$ (top).

Ch.-H. Fischer, M.C. Lux-Steiner, H.-J. Muffler, M. Bär, M.C. Lux-Steiner (SE2.08 Buffer Layers, Alternative Thin-film Technology), C. Kelch, M. Kirsch (SE2.05 Chalcopyrite Solar Cells), S. Fiechter (SE5 Solar Energetics) in collaboration with L. Weinhardt, C. Heske, E. Umbach, (Universität Würzburg); B. Leupoldt (Fraunhofer Institut Werkstoff- und Strahltechnik, Dresden); F. Karg, S.Zweigart (Siemens&Shell Solar GmbH, München); B. Gay (Siemens Solar Industries, Camarillo USA)

Eta-solar cell and other applications

Eta-solar cells

In the eta-cells project we aim at the fabrication of solar cells with extremely thin absorber layers. Sufficient absorbance in these cells is ensured by depositing the absorber on a deeply structured substrate with a high surface enlargement. Strong light trapping and short transport paths in the absorber are the key features in this type of cell. Fig. 1a shows a model for such a cell.

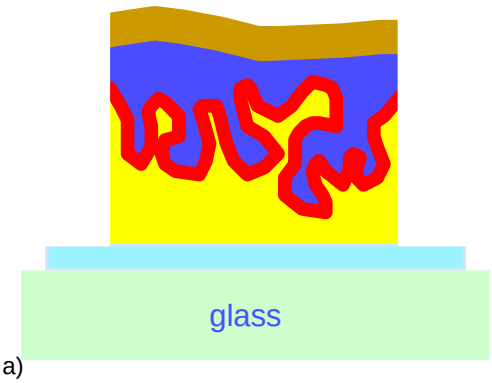

a)

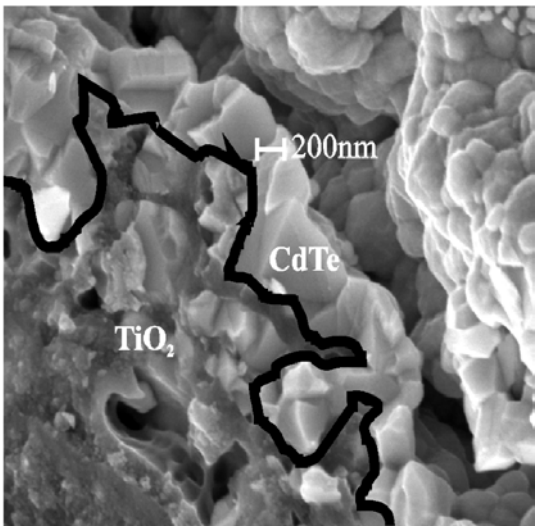

b)

Fig. 1: a) Model of the envisioned eta-solar cell with a thin absorber (red) and back contact (blue) deposited on a nano- or microstructured substrate (yellow). b) ~200nm nano-crystalline CdTe-layer on micro-porous TiO_2 substrate. EDX and electron scattering contrast allow to distinguish the two materials, which are in intimate structural and electrical contact.

So far, the most promising device consists of a CdTe absorber layer deposited in electrodeposition on a micro-porous TiO_2 substrate. Contacts are provided by highly conducting SnO_2/glass on the TiO_2 light entry side and an Au or graphite layer at the back. The CdTe consists of a nano-crystalline layer of approximately 150 nm thickness covering the TO_2 surface as a continuous film.

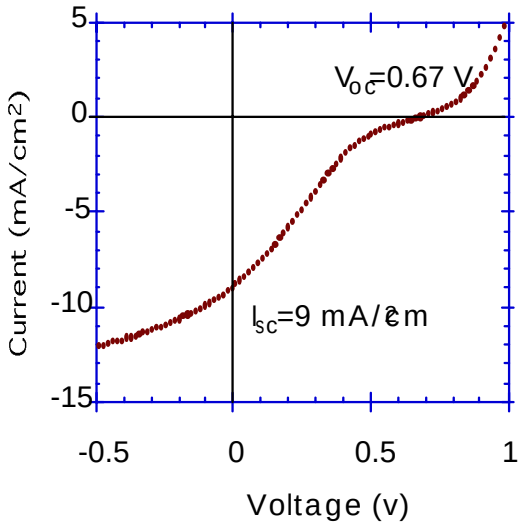

a)

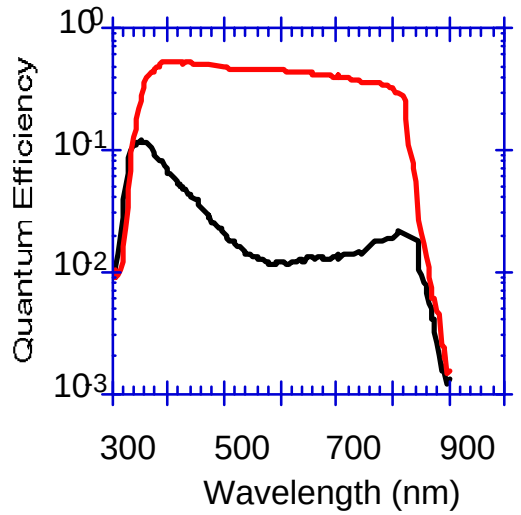

b)

Fig. 2: a) I-V characteristic of eta-cell under 100 mW AM1 illumination. b) Comparison of quantum efficiency for eta-cell (red) and planar reference (black).

A micrograph of the TiO_2/CdTe interface is shown in Fig. 1b. An optimized cell of this type has produced an open-circuit voltage of 0.67 V and a short-circuit current of 9 mA/cm^2 (Fig. 2). When compared to a planar reference cell with CdTe of the same quality and the same total thickness, the eta-cell arrangement shows much superior performance. As shown in Fig. 2b, the quantum efficiency is approximately a factor of 10 higher in the eta-cell than in the planar cell.

In the last year we have carried out a detailed optical, electrical and structural characterization of this cell [1]. XPS/UPS measurements indicated a surprisingly large conduction band off-set of 0.6 eV at the CdTe/TiO_2 interface, which leads to a comparably small band-bending. Numerical simulation of

the electron transport across the interface indicates that the poor fill factor, which presently limits the efficiency of the cell, is a consequence of the small band bending. We will therefore have to address the problem of "band engineering" at nano-structured interfaces in the near future.
A promising alternative to the porous morphology used so far, appears to be given by substrates with columnar crystallites, since the electron transport path will involve fewer grain boundaries. We recently developed ZnO layers with nearly vertically aligned, single-crystalline columns. In these substrates we found electron mobilities as high as 20 cm^2/Vs, confirming this expectation. We therefore started work to implement columnar morphologies in several chalcogenide-based compounds.

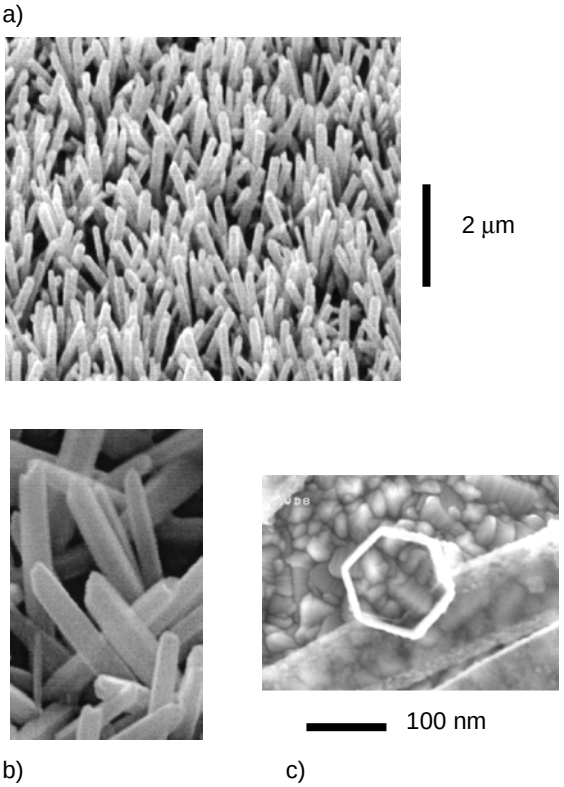

Fig. 3: a) Scanning electron micrograph of single-crystalline ZnO columns. b) The same at higher magnification. c) Hexagonally shaped ZnS tubes prepared by ion exchange from ZnO columns and subsequent etching. The image shows one vertical and two horizontal tubes.

Using sequential ion exchange we were able to transfer the columnar morphology of the ZnO substrates to several other compound semiconductors, such as ZnS, Ag_2S, Cu_2S, Bi_2S_3, Sb_2S_3 and others [2]. We also learnt to manipulate these nano-structures to some extent. Fig. 3 shows hexagonal columnar ZnO crystallites and a hexagonally shaped nano-tube of Zincblende ZnS, which was prepared by partial conversion of a ZnO column and subsequent etching of the core. The tube has a diameter of 150 nm, a wall thickness of 15 nm and can have lengths up to 2 μm.

Other applications

Our experience in nano-scale semiconductor deposition also lends itself to the preparation of devices on flexible substrate. Using irradiation by fast heavy ions and subsequent etching, narrow hollow cylinders can be prepared in μm thick polymer foils. We have applied electrodeposition to fill these cylinders with semiconductor compounds [3]. Fig. 4 shows free-standing CuSCN cylinders which resulted from this work. In this case the CuSCN columns are exposed. While these exposed columns could be used as substrates in solar cell applications, the embedded columns may also become part of a flexible electronic device.

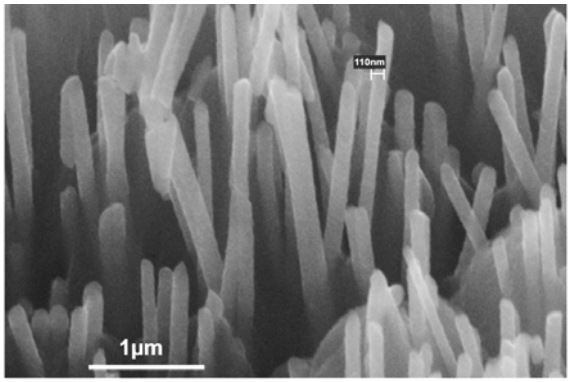

Fig. 4: Free-standing CuSCN columns grown in flexible polymer foils.

References

[1] C. Grasso, K. Ernst, R. Könenkamp, M. Burgelman, M. C. Lux-Steiner, Proc. PVSEC, München 2001

[2] L. Dloczik, R. Engelhardt, K. Ernst, S. Fiechter, I. Sieber, R. Könenkamp, Appl. Phys. Lett. 78, 3687 (2001)

[3] R. Engelhardt and R. Könenkamp, J. Appl. Phys. 90, 4287 (2001)

R. Könenkamp, K. Ernst, L. Dloczik, J. Chen, R. Engelhardt
(SE2.07 Eta-cell)

Alignment of the endohedral fullerenes N@C_{60} and N@C_{70} in liquid crystals

Endohedral fullerenes [1] are envisaged to serve as quantum bit carriers in a quantum computer design [2,3]. For this application, an alignment of fullerene chains is required which is naturally achieved by embedding them in a liquid crystal matrix.
N@C_{60} and N@C_{70} in solution show a three line spectrum in EPR due to the hyperfine interaction of the electrons with the nuclear spin I = 1 of ^{14}N (top of Fig.1). Since the electron spin of nitrogen is S = 3/2, each of these hyperfine lines consists by itself again of three lines which are degenerate for a spherically symmetric electron distribution. However, for non-spherical atoms the degeneracy is lifted and the three lines become visible (see lower part of Fig. 1).

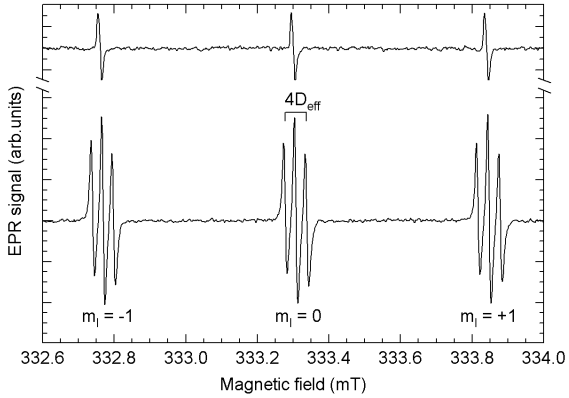

Fig. 1: EPR spectrum of N@C_{70} in toluene solution (upper graph) and N@C_{70} in MBBA liquid crystal (lower graph) at 299 K. The magnetic quantum number m_I of the nuclear spin I = 1 and the splitting of the outer lines by 4D_{eff} (see text) for the m_I = 0 hyperfine line are indicated.

For an axially symmetric interaction and high external field, the splitting $\Delta\nu$ (separation between two successive peaks in each hyperfine multiplet) in the EPR spectrum can be represented as $\Delta\nu = 2\ D_{eff}$, where D_{eff} is an effective interaction for this specific orientation. The fine structure interaction splits each hyperfine line into three lines, one at the original position and one shifted to lower and one to higher fields. Fig. 1 shows this additional line splitting for N@C_{70} in the liquid crystal MBBA [4].
C_{60}, other than C_{70}, has no natural axis for alignment in a liquid crystal. However, as Fig. 2 shows, there is also a splitting of the EPR line, and thus an alignment for N@C_{60}. The observed splitting shows that the spin density distribution of the enclosed nitrogen atom in C_{60} slightly deviates from spherical. The explanation is that the contact of C_{60} with the aligned liquid crystal molecules induces a slight deformation of the electron shell of C_{60}, which in turn affects the electron density distribution of the enclosed nitrogen.

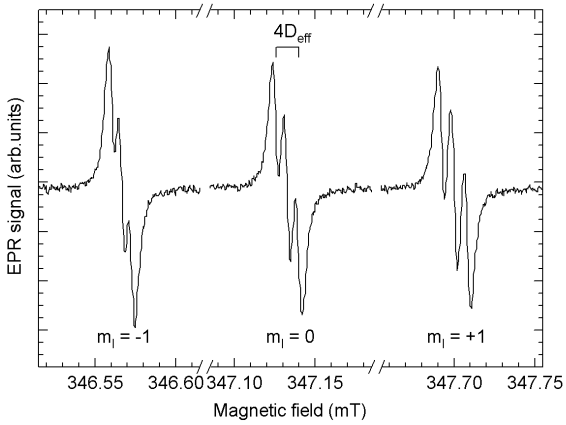

Fig. 2: EPR spectrum of N@C_{60} in MBBA liquid crystal at 296 K. Note that the field axis is interrupted between the lines in order to emphasise the splitting. The magnetic quantum number m_I of the nuclear spin I = 1 and the splitting of the outer lines by 4D_{eff} (see text) for the m_I = 0 hyperfine line are indicated.

The alignment of the endohedral fullerenes in a liquid crystal matrix is of great importance in connection with quantum computing. There, one can construct by chemical means a chain of endohedral fullerenes, e.g. dimers [5] or polymers, and embed them in a liquid crystal. Since the magnetic interaction between the fullerenes is dipolar, the arrangement in a chain and the orientation with respect to the external field ensures that the interaction is unique and even changeable if the angle between the chain axis and the external field is varied. Since the fullerenes are diluted in the liquid crystal, the inter-chain interaction is negligible as required for independent small qubit assemblies.

References

[1] T. Almeida Murphy, T. Pawlik, A. Weidinger, M. Höhne, R. Alcala, J.M. Spaeth, Phys. Rev. Lett. 77 (1996) 1075

[2] W. Harneit, M. Waiblinger, K. Lips, S. Makarov, A. Weidinger, AIP Conf. Proc. 544 (2000) 207

[3] W. Harneit, M. Waiblinger, K. Lips, C. Meyer, A. Weidinger, and J. Twamley, in Experimental Implementation of Quantum Computation, edited by R.G. Clark (Rinton Press Inc., Princeton, NJ, 2001) 38

[4] H. Kelker, R. Hatz, Handbook of Liquid Crystals, Verlag Chemie (Weinheim, Germany, 1980)

[5] B. Goedde, M. Waiblinger, P. Jakes, N. Weiden, K.-P. Dinse, A. Weidinger, Chem. Phys. Lett. 334 (2001) 12

C. Meyer, W. Harneit, R. Döring, B. Mertesacker, K. Lips, A. Weidinger (SE2.02 Fullerenes) n collaboration with P. Jakes, K.P. Dinse (TU Darmstadt)

Synchrotron-diagnostics for cost-efficient photovoltaic devices (CISSY)

Project Goals

This joint project with Universität Würzburg, Siemens & Shell Solar and BESSY aims at the development of optimized chalcopyrite thin film solar cells (CIGSSe). This is achieved through an interplay between various spectroscopic analysis methods and preparation at small and production scale. An experimental set-up is installed at the BESSY synchrotron, which combines sophisticated spectroscopy with the preparation of buffer, window, and absorber layers. Detailed experimental knowledge will be gained about the chemical and electronic structure of buried interfaces, which is of particular importance for the electrical performance of the cells. The results of this work will then directly be fed back into solar cell fabrication, allowing an optimization far beyond the common trial-and-error approach.

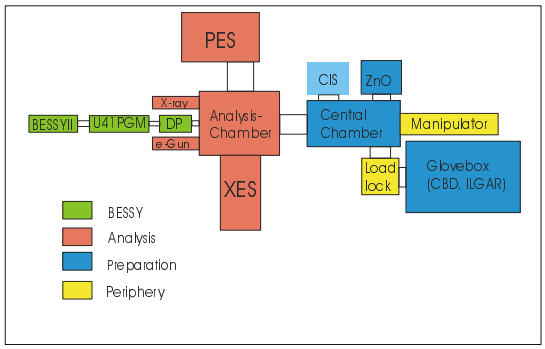

Fig. 1: Block diagram of the experimental endstation (CIS: chalcopyrite module, planned; ILGAR: Ion Layer Gas Reaction; CBD: Chemical Bath Deposition)

Experimental set-up and current status

The set-up of the apparatus is schematically shown in Fig. 1. It consists of an analysis chamber containing the spectrometers, a central main chamber for simple preparation procedures, a sample manipulator, a chamber for ZnO sputter deposition, a glove box for wet-chemical processes, and a load-lock system. The analysis chamber will house an XES 300 Soft X-ray Emission Spectrometer and a high-resolution electron analyzer. The central chamber allows ion sputter treatments, sample annealing and sample storage. Various preparation procedures will be implemented into several side-chambers: chemical conditioning of the absorber, including etching and ion exchange treatments, chemical bath deposition (CBD), ion layer gas reaction (ILGAR) for deposition of buffer layers, and sputtering deposition of selected window layers. The experimental set-up is complete and initial experiments have been performed: various layers were prepared both on glass and CIGSSe absorbers using chemical methods like ILGAR and CBD. An explorative spectroscopic analysis was carried out at the Advanced Light Source (ALS) in Berkeley.

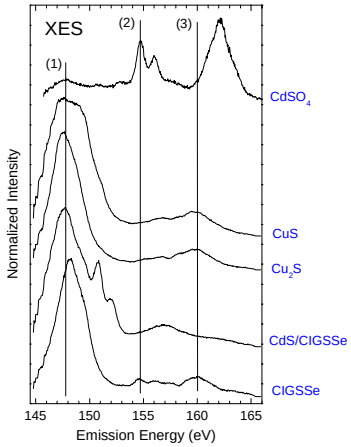

Fig. 2: XES-spectra of different sulfur compounds with characteristic peaks. The marked peaks are attributed to the following electronic transitions:
(1): S 3s → S 2p (sulfide environment)
(2): S 3s → S 2p SO_x (x≤2)
(3): Cu 3d → S 2p Cu-S bonds

The XES-spectra (Fig. 2) show characteristic peaks which identify the local chemical environment of the sulfur atoms. The spectra in Fig. 3 were taken on a $Cu(In,Ga)(S,Se)_2$-sample in contact with water using a wet cell with a polymide window. With increasing exposure to the x-ray beam the data indicate a formation of sulfate.

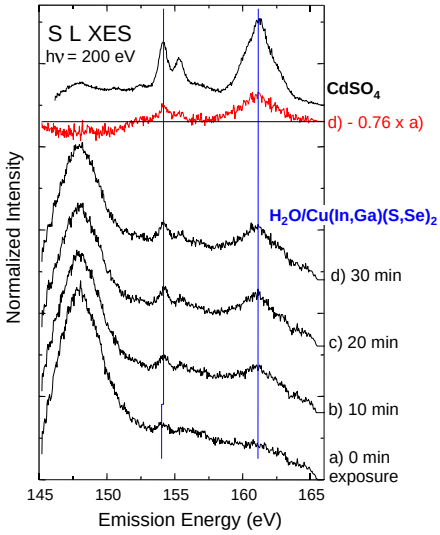

Fig. 3: S Lα-XES spectra of a $Cu(In,Ga)(S,Se)_2$-sample in contact with water after different exposure times compared to $CdSO_4$ (above).

M. Ch. Lux-Steiner, Ch. H. Fischer, A. Grimm, I. Kötschau, I. Lauermann, J. Reichard, S. Sokoll (SE2.08 Synchrotron Analytics) in collaboration with E. Umbach, C. Heske (Universität Würzburg); W. Gudat, Ch. Jung (BESSY Berlin) and F. Karg (Siemens&Shell Solar, München)

Department

SE3 Technology

Chalcopyrite solar cells and monolithically integrated test modules

This project aims at the development of a technological process for the preparation of modules and solar cells based on the chalcopyrite semiconductor $CuInS_2$ with an efficiency of 10 % and above. Development targets are: reproduceable efficiency, high process and material yield, compatibility with the specifications of inexpensive substrates as well as suitability for industrial environment (scalability and throughput). The project forms the scientific basis for the scaling-up effort of a start-up company. The baseline supports internal and external research on $CuInS_2$ solar cells and on other chalcopyrite semiconductors.

Producing a ternary compound semiconductor on large areas requires to overcome the stoichiometry problem. The process developed at HMI is specific in the sense that it uses growth of the chalcopyrite $CuInS_2$ from non-stoichiometric precursors (Cu/In>1) and the chemical stoichiometry adjustment by chemically etching of a surplus CuS layer after sulfurization [1]. This approach results in an inherent process stability as will be shown below.

Fig. 1 gives the dependence of the open circuit voltage and fill factor on top temperature (Fig. 1a) and the amount of sulfur in the sulfurization containment (Fig. 1b). A broad maximum in the temperature dependence is found. Also the amount of added elemental sulfur can be varied in a wide range. The latter result reflects the well known property of chalcopyrite materials which is the self-adjustance of the group VI element. A plot of the cell data vs the deposited Cu/In ratio is given in Fig. 1(c). The Cu/In ratio can be varied from about 1.2 up to 1.8 without a strong effect on the cell parameters.

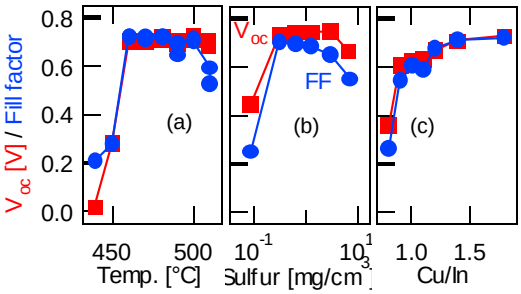

Fig.: 1 Dependence of V_{oc} and fill factor on the RTP process parameter top temperature (a) amount of sulfur (b) and precursor Cu/In ratio (c)

With aid of the $CuInS_2$ baseline the reproducibility of the process was investigated. Fig. 2 gives a direct print-out of the baseline performance over a period of 6 months. For 114 samples processed in this period, a narrow distribution of the cell efficiency peaking at 10.7 % (total area) has been found. The absolute FWHM of this curve is 1.35 %. In accordance with physical arguments, the chemical stoichiometry adjustment of the absorber layer (etching of Cu-rich prepared absorber) is the key factor of the process robustness.

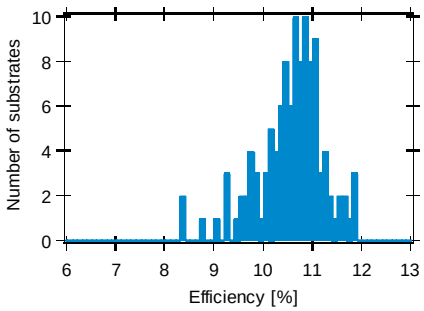

Fig. 2: Direct print-out of the $CuInS_2$ cell baseline statistic from the period Jan-Jul 2001 showing the efficiency distribution from 114 processed samples. Each data point represents the average of up to 6 cells (0.5 cm^2) on one glass substrate

The $CuInS_2$ cell base line has recently been extended to a module baseline (5×5 cm^2, 20 cm^2 aperture area). The module baseline currently delivers efficiencies up to 10.2 % on an aperture area basis. An encapsulated module sample is shown in Fig. 3. Parameters of the champion module are V_{oc}=5.1 V, j_{sc}=21 mA cm^{-2} , FF=66.6 %. Less efficient modules still suffer from inferior fill factors. Fill factors less than 65 % could each be related to pin holes or shunts mainly at the interconnects by use of lock-in thermography.

A critical dimension of integrated modules is the cell width. Two general dependencies have to be considered: A too small cell width increases the relative area of the interconnect, thereby increasing current losses. A too large cell width increases the series resistance due the sheet resistance of the window layer. Using test structures, an optimum cell width of 6 mm has been derived based on the currently realized material parameters. In order to increase this cell width, these material parameters have to be newly optimized; for instance the sheet resistances have to be reduced.

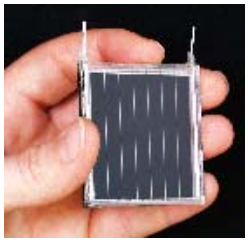

Fig.3: Encapsulated $CuInS_2$-based monolithically integrated test module

References

[1] R. Scheer, T. Walter, H.W. Schock, M.L. Fearheiley and H.J. Lewerenz, Appl. Phys. Lett. **63**, 3294 (1993)

J. Klaer, I. Luck, A. Boden, A. Werner, I. Gavilanes-Perez, R. Klenk, R. Scheer (SE3.01a Monolithically Integrated Test Modules)

Quality control and reliability of thin film solar cells

For a reliable production process of thin film solar cells, quality control of different constituents of the cells are desired. Concerning quality assessment of chalcopyrite thin films there is a general lack of appropriate methods. This is mostly due to a missing correlation to solar cell parameters. In order to assess the quality of the $CuInS_2$ absorber layer, Raman spectroscopy has been tested. This method is particularly interesting as it allows fast access to absorber properties at room temperature without fabricating complete solar cells.
In collaboration with the University of Barcelona (UB), a Raman data base from samples with different structural quality has been generated in order to study the influence of film properties on the Raman modes. These experiments aim at establishing a quality assessment method for chalcopyrite absorbers. Therefore, a relation between solar cell parameters and structural data is the final goal. Fig. 4 shows Raman spectra of two $CuInS_2$ thin films prepared on Si(111). The totally symmetric chalcopyrite A1 mode can be observed together with additional modes at 60 cm^{-1} and 305 cm^{-1}. Since the structural quality as well as the solar cell parameters of Cu-poor films are inferior than those of Cu-rich films, the presence of the additional modes, which is more intense for Cu-poor films, can tentatively be interpreted as a marker for crystal defects. The origin of these modes, however, previously was not known.

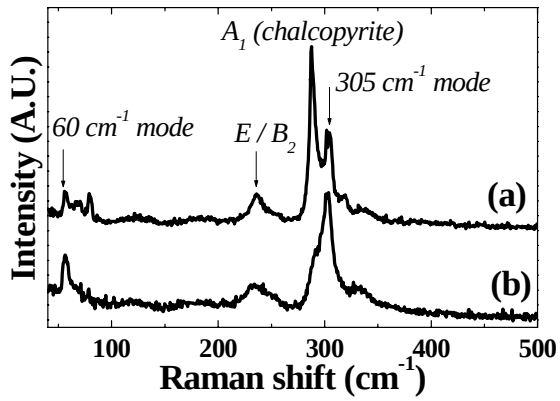

Fig.4: Raman spectra of Cu rich (Cu/In>1, curve a) and Cu poor (Cu/In<1, curve b) epitaxial films showing the presence of the additional non-chalcopyrite bands at 60 cm^{-1} and 305 cm^{-1}.

An assignment of the additional modes was recently achieved by a HMI-UB collaboration. Samples epitaxially grown on Si(111) were investigated using Raman spectroscopy and XRD. In XRD, the occurrence of the $CuInS_2$ (100) diffraction was observed which is related to a defect ordering of cations in the lattice. This so-called CuAu ordering has been theoretically predicted [2] and has first been found by our group [3]. Combined XRD and Raman data of films with different structural quality (due to the deposition temperature) are given in Fig.5. Clearly, a relation between the CuAu related XRD peak and the additional Raman modes are revealed [4]. Hence, the additional Raman modes are due to the defect ordering of CuAu. First principle calculations support this interpretation [4]. More detailed analysis showed that the FWHM of the chalcopyrite A1 mode is also correlated with the CuAu content. This is important for samples which are apt for highly efficient solar cells having only a small CuAu Raman intensity. The next step was to investigate the correlation between the CuAu related Raman intensity of different samples and the solar cell parameters. Preliminary results indeed point out this inverse relation: the lower the CuAu related Raman features the higher the cell's open circuit voltage. This correlation may be used for later material assessment and the prediction of solar cell efficiency based on the quality of the constituent.

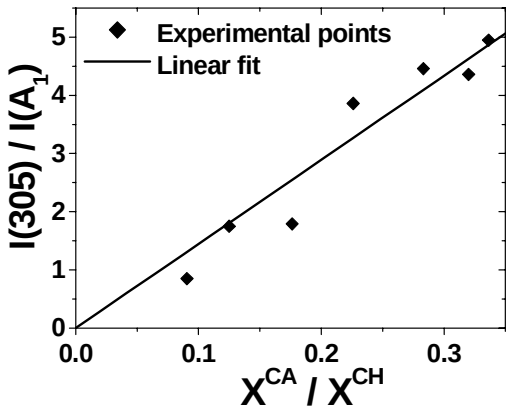

Fig. 5: Correlation between Raman relative intensity of the 305 cm^{-1} mode and the estimated amount of Cu-Au ordered phase.

References

[2] S.-H. Wei, S.B. Zhang and A. Zunger, Phys. Rev. B **59**, R2478 (1999)

[3] D.S. Su, W. Neumann, R. Hunger, P. Schubert-Bischoff, M. Giersig, H.J. Lewerenz, R. Scheer and E. Zeitler, Appl. Phys. Lett. **73**, 785 (1998).

[4] J. Alvarez-Garcia, A. Perez-Rodriguez, B. Barcones, A. Romano-Rodriguez, J.R. Morante, A. Janotti, S.-H. Wei and R. Scheer, Appl. Phys. Lett. **80**, 562 (2002)

R. Scheer, E. Rudigier, A. Perez-Rodriguez, A. Romano-Rodriguez, J. Alvarez-Garcia, B. Barcones (SE3.01b Quality Control and Reliability of Thin-film Solar Cells)

In-situ process monitoring

In the last annual report, we presented the method of diffuse laser light scattering (LLS) for monitoring the sulfurization process of metallic Cu/In precursor layers. LLS transients recorded during the sulfurization showed distinct intensity features which were tentatively assigned to phase transitions or previously could not be related to any kind of precursor transformation at all. The task thus was to find out the structural origin of LLS transient features in order to establish this method for a future industrial process control.

LLS experiments have been conducted at Hasylab while simultaneously recording energy dispersive X-ray diffraction (EDXRD) spectra. With a time resolution of 15 s, EDXRD is able to resolve phase transitions which occur during the sulfurization of metallic Cu/In layers. Fig. 6 gives a series of EDXRD spectra recorded during the sulfurization of the metallic precursor. The graphs depict the time evolution of several peaks during a sulfurization experiments (bottom trace represents the ramp-up start). Clearly, the evolution of the $CuInS_2$ (112) diffraction is visible. This diffraction occurs already in the ramp-up period of the substrate and comes along with a strong decrease of the LLS intensity.

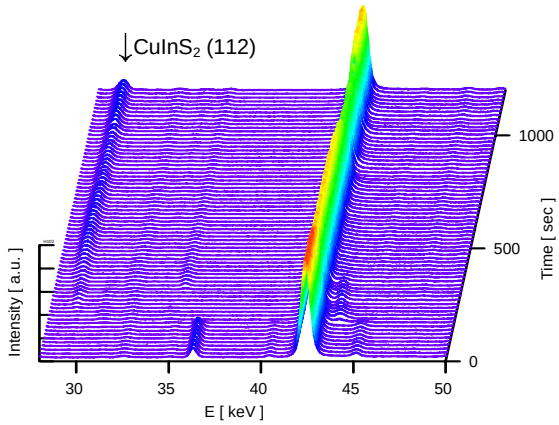

Fig.6: Time series of EDXRD spectra during the sulfurization of a Cu-rich CuIn precursor on a molybdenum coated soda lime glass, 5 min heat up time, T_{Sub} = 500 °C

The area of the diffraction peaks is determined for each spectrum in Fig. 6 and is plotted as a function of time in Fig. 7. The graph also contains the substrate temperature during the course of the sulfurization process. Due to the penetration depth of X-rays in the investigated wavelength range, the area of the diffraction peaks can in a first approximation be considered as an indicator of phase volume fraction. From Fig. 7, a variety of phase transitions can be appreciated. These are intermetallic transitions and metal-semiconductor transitions. In addition, the position of the EDXRD peaks can be used to determine stress development in the layers. Fig. 7 gives the example of the Mo (110) lattice spacing as a function of time.

The combination of both optical and structural techniques has allowed the assignment of the following laser light transient features. The assignments, derived from Fig. 7, were:

α: $CuIn_2 \rightarrow Cu_{11}In_9$
β: surfacial $CuInS_2$
χ: $Cu_{11}In_9 \rightarrow Cu_{16}In_9$

These assignments are very useful for the application of the LLS method for process control and were the basis for a patent application for an optically controlled chalcogenization process. We prepared solar cells from $CuInS_2$ films formed in the *in-situ* EDXRD chamber. Since they exhibited up to 10.6% efficiency, the relevance of these model experiments is demonstrated.

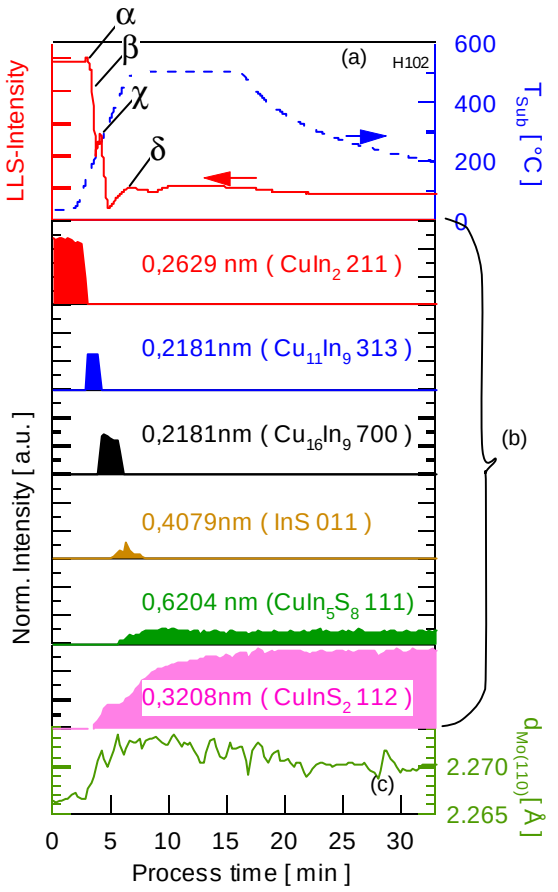

Fig. 7: (a) Temperature profile and LLS intensity, (b) intensity of characteristic diffraction peaks and (c) EDXRD lattice spacings of Mo from the annealing of a Cu,In precursor (Cu/In=0.7) on Mo/glass. Phases identified are given in parenthesis. Details of the process are 5 min heating-up, 10 min hold, and passive cooling. The d-spacing of the Mo 110 peak reveals stress release in the ramp-up period.

Ch. Pietzker, E. Rudigier, R. Scheer
(SE3.01c In-situ Process Control and Doping)

Doping

The formation of local pn-junctions in chalcopyrite thin films would allow the combination of solar cells and electronics on a single substrate. However, this formation was previously not possible. In a joint research effort, the Weizmann Institute of Science, Israel, and HMI have recently invented the method of electric field induced junction formation.
Epitaxial layers of $CuInSe_2$ grown on n-type Si(111) were mounted on a base electrode. An electric field was applied to the surface of the $CuInSe_2$ film via a second contact which is a movable tungsten tip. Beyond a certain negative threshold voltage, a pn-junction was created in the film and a laterally extended junction could be scribed by moving the tip [5]. The p- and n-regions are laterally formed in the layer as can be appreciated from the EBIC image of Fig.8 where bright areas represent the n-type region. By scribing the junction up to a predefined gold pad on the $CuInSe_2$ surface, it was possible to contact the junction.
The origin of the electric field induced junctions can at the moment only tentatively be described: Mobile Cu ions move towards the tip and form an n-type region in the direct vicinity of the tip. In the former host area of the Cu atoms Cu vacancies are formed and this area is converted into a p^+-type region. The basic idea of the process can be apprehended from Fig.9. The process is temperature activated by the current flow from the tip to the back contact. Since the $CuInSe_2$/Si interface forms a blocking contact, lateral current densities occur.
The persistence of the formed junctions has been tested one year after formation. No relaxation of the pn-junction was found. Also the surface of the $CuInSe_2$ layer was proven to be unaffected by the scribing process. The next step will be the application of the electric field through rigid contacts. A patent application has been filed.

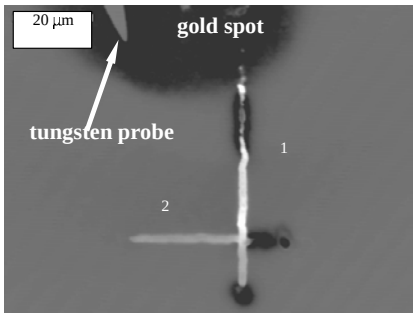

Fig.8: EBIC image of a pn-junction scribed into the surface of a $CuInSe_2$ thin film deposited on Si(111). Two perpendicular junction scribes were performed, one being connected to a gold spot on top of the surface. The EBIC current is flowing through the n-region of the pn-junction to the gold spot. Thus the n-region is electrically connected.

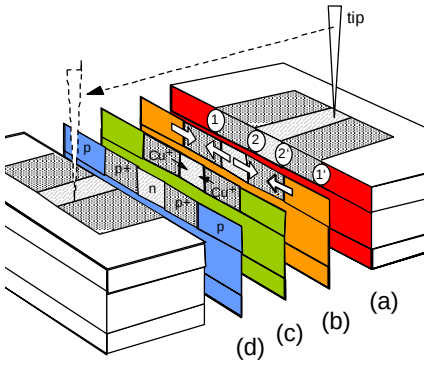

Fig.9 : Tentative model of junction region creation within $CuInSe_2$ epilayers. (a) Four junctions can be derived. (b) Electric fields are driving the EBIC currents. Electric field vectors can be drawn between dashed and dotted as well as dotted and white zones. The white zone is the pristine p-$CuInSe_2$ layer. (c) Application of negative bias (-100 V) leads to migration of Cu^+ ions towards the tip. There Cu_i defects act as donors forming an n-type region (d). Cu depletion leads to V_{Cu} in adjacent zones (dotted) which become more p-type. As a consequence, junction regions are formed between depleted and non-depleted zones. Moving the biased tip creates a patterned junction within the sample.

References

[5] K. Gartsman, D. Cahen and R. Scheer, Appl. Phys. Lett. **79**, 2919 (2001)

R. Scheer, K. Gartsman
(SE3.01c In-situ Process Control and Doping)

Department

SE4 Dynamics of Interfacial Reactions

Time-resolved dynamics of hot electrons in InP(100)

The actual efficiency of a solar cell is always significantly lower than the maximum value derived from thermodynamic considerations. This holds true also for the most efficient solar cells (above 30 percent conversion efficiency) that can be realized with III-V materials. Efficient recombination paths, i.e. loss mechanisms, are known to arise for III-V materials at surfaces and interfaces. Hitherto, such loss mechanisms have generally been considered only for thermalized charge carriers on longer time scales, i.e. nano-seconds or longer. Recombination of thermalized charge carriers can be studied with several conventional measuring techniques. It is well known, however, that already hot carriers can reach a nearby surface or interface prior to thermalization. This holds true in particular in III-V materials with high absorption coefficients and good transport properties. The surface of a III-V-semiconductor in contact with ultra-high-vacuum is the simplest interface that can be realized with different atomic reconstructions. The pioneering work of Bokor [1] and Haight [2] has shown that interfacial reactions of hot carriers can be studied employing time-resolved two-photon-photoemission (2PPE). The principle of this 2PPE method is illustrated in Fig.1. Electrons are photo-emitted into vacuum and the distribution over kinetic energy is measured. A narrow kinetic energy window can be addressed (in our case about 100 meV wide) that probes the corresponding intermediate states (Fig.1). Time-resolution is achieved by varying the time-delay between the two consecutive laser pulses. This way, the dynamics of hot carriers are time-resolved for specific intermediate states. The latter are occupied due to photon absorption and are emptied via subsequent relaxation and scattering processes. Fig.2 shows the disappearance of hot electrons from intermediate states about 1.15eV above the lower edge of the conduction band of InP(100) [3]. Hot electrons were generated by the first femtosecond laser pulse (2.52eV photon energy) and photo-emitted by the second laser pulse (4.66eV photon energy) with variable delay. The crystal surface was prepared with an ordered In-rich reconstruction. The instrumental cross correlation function (inset in Fig.2) was measured as two-photon-photoemission involving virtual intermediate states at the Cu(111) surface. The main part of the signal in Fig.2 decayed faster than our presently available time resolution of about 30fs. The origin of the slower tail is not yet clear.

One possibility is the return of hot electrons back to the Γ-valley, where the intermediate states are probed, from different k-states where they had been scattered after being generated initially by the first laser pulse near the Γ-valley.

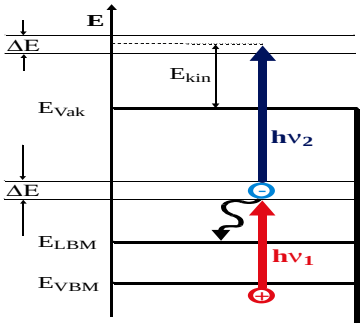

Fig.1: Illustration of femtosecond two-photon-photoemission. The first laser pulse (photon energy hν1) lifts electrons to unoccupied electronic states. The second laser pulse (photon energy hν2) promotes these electrons into vacuum.

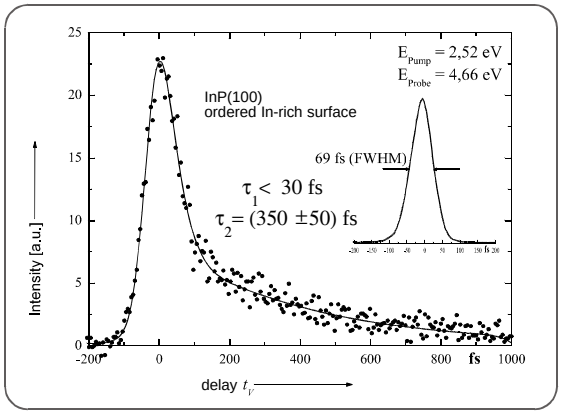

Fig.2: Decay of hot electrons about 1.15eV above the lower conduction band edge of InP measured via femtosecond two-photon-photo-emission.

References

[1] J. Bokor, Science 246 (1989) 1130

[2] R. Haight, Chem. Phys. 205 (1996) 231

[3] L. Töben, PhD Thesis, Technical University of Berlin, 2002

L. Töben, R. Eichberger, L. Gundlach, T. Hannappel, K. Möller, R. Ernstorfer, F. Willig
(SE4.01 Dynamics of Light-induced Charge Transfer)

Preparation and characterization of the n-SnO_2/p-InP heterocontact

Formation of the heterocontact n-SnO_2/p-InP(100) via spraypyrolysis was accomplished without excessive loss of phosphorus. InP develops a deficit in its phosphorus content once it is brought to a temperature higher than the congruent evap-oration temperature (350°C). Such a high tem-perature is required, however, for forming the contact with n-SnO_2 via spraypyrolysis. Its simplicity makes the latter preparation technique attractive. If an excess of phosphorus leaves the InP wafer In droplets will be left behind on the surface. They can give rise to excessive recombination losses for the photocurrent. It was at hand to minimize the time during which InP is exposed to the high tem-perature. It turned out that preventing excessive loss of phosphorus required a further protective preparation step. Prior to forming the heterocontact via spraypyrolysis a few atomic layers of Sn were deposited onto the freshly grown surface of the InP wafer. For this preparation step the group's patented contamination free sample transfer had to be employed [1]. Fig. 1 shows TEM images of cross sectional preparations. The formation of an unwanted thick amorphous layer of mixed phosphate and oxide can be seen in panel a if the Sn layer was absent. In contrast, this thick amorphous layer was not formed (panel b) if Sn was deposited prior to applying spraypyrolysis [2]. Sn forms chemical compounds with phosphorus that can stop the loss of phosphorus. A possible excess of Sn is converted to SnO_2 during spraypyrolysis. The photo-electrical behavior of the heterointerface improved significantly for the interface illustrated in panel b compared to that of panel a. Improvements were seen in the onset voltage of the photocurrent and in the capacitance determined from a Mott-Schottky plot. An abrupt interface was suggested firstly by SIMS signals, secondly by the spectral dependence of the photocurrent at the blue edge, and thirdly by the spatial onset of an EBIC signal.

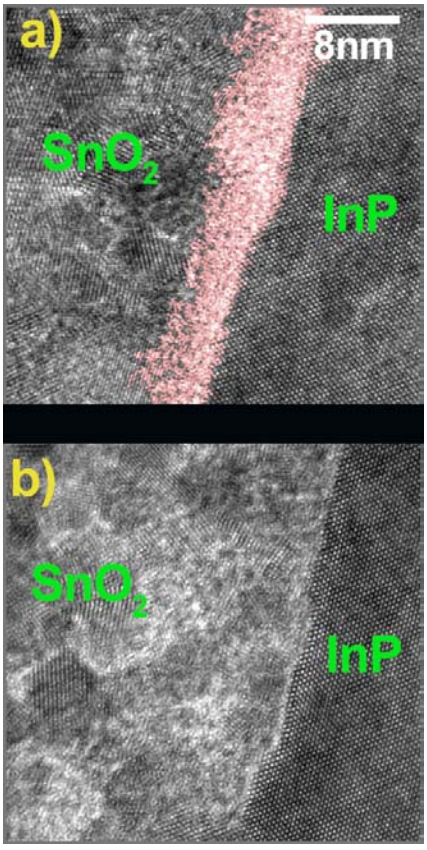

Fig. 1: TEM images of cross sections of the hetero-interface: SnO2:F/InP:Zn(100) in the absence (panel a) and presence (panel B) of a thin layer of Sn.

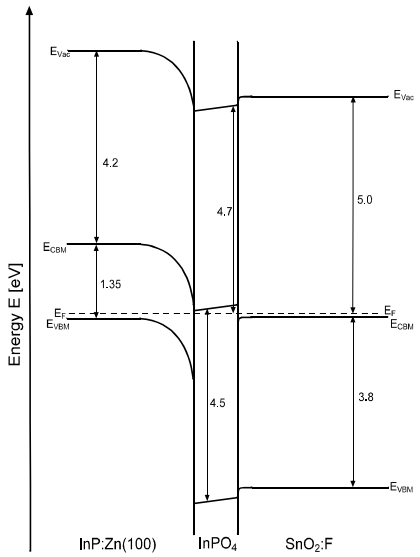

Fig. 2: Banddiagram for p-doped(Zn) InP(100) covered by an amorphous layer of mixed oxide/phosphate (labeled InPO4 here, compare panel a in Fig.1) followed by a polycrystalline layer of n-doped SnO2:F.

The banddiagram shown in Fig. 2 is in agreement with the measured electrical signals. The band bending is already established at the p-InP/vacuum interface irrespective of whether the surface is P-terminated or In-terminated. The corresponding Fermi-level pinning has been found to be very robust and to remain at the surface independent of the material that is deposited on top.

References
[1] T. Hannappel, F. Willig, DPMA Munich, Patent No. 19837851
[2] Dirk Herrmann, PhD Thesis, Technical University of Berlin, 2001

D. Herrmann, L. Toeben, K. Schwarzburg, T. Hannappel, M. Neges, K. Möller, U. Bloeck, F. Willig (SE4.02 Preparation and Characterization of III-V-Semiconductors)

Department

SE5 Solar Energetics

Platinum-free catalysts for the reduction of oxygen

The aim of this project is to develop platinum free catalysts for the electroreduction of oxygen in acidic media and to optimize them with respect to their catalytic activity and morphology for an application as gas-diffusion-cathode in proton exchange membrane (PEM) fuel cells. Starting from own results [1], we were able to improve a Ru-Se based catalyst by developing several new preparation strategies and by optimizing the catalysts composition. Fig. 1 shows the achieved progress indicated by H_2-PEM fuel cell measurements. Although the catalytic activity of the best preparation (colloidal techniques) remained below the output characteristic of platinum using hydrogen as fuel the Ru-Se catalyst has advantages using methanol as fuel in Direct Methanol Fuel Cells (DMFCs). This is because the Ru-Se catalyst is stable against depolarization by methanol. Due to the leaking of methanol from the anode to the cathode in direct methanol fuel cells the Ru-Se catalyst exhibits a better performance than platinum. This was verified under laboratory conditions. DMFC measurements under industrial conditions are in progress.

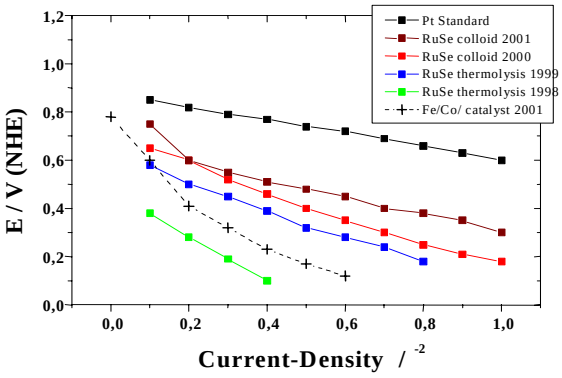

Fig. 1: Current-voltage-characteristic of H_2-PEM fuel cells using Ru-Se and Fe/Co catalysts at the cathode site (cathode: C / Ru_xSe_y (20%Ru / C, load 0.14mg/cm^2); Fe/Co (5 %Co/C, load 0,2mg/cm^2) operation pressure 3bar of compressed air; anode: Pt, load 4mg/cm^2, fuel: H_2; operation temperature: 80°C, active area: 50cm^2.

Rotating disc electrode (RDE) experiments, applying a Fe-Co-N catalyst, revealed that the kinetic parameters are close to those of platinum (Fig.2). However under fuel cell conditions, the efficiencies remained up to now behind the platinum standard (dotted line in Fig. 1) presumably due to the coarse mesoscopic shape of the carbon supported catalyst and the relative low catalyst-loading onto the carbon support. The aim of our work is to develop new preparation strategies to overcome this disadvantage.

Ruthenium based catalysts

It was demonstrated in earlier work from the department (Alonso-Vante and Solorza)[1] that catalysts based on Ru, Se and Mo can be used for the oxygen reduction in acidic solutions. The catalysts were prepared from $Ru_3(CO)_{12}$ and $Mo(CO)_6$ by thermolysis in a selenium saturated organic solution. Carbon supported catalysts could be formed by addition of carbon black to the reaction mixture. The parameters of this preparation procedure (several organic precursors and organic solvents, variation of the selenium concentration, subsequent activation by heat treatment steps) to optimize the catalytic activity and the morphology of the Ru-Se catalyst were investigated.

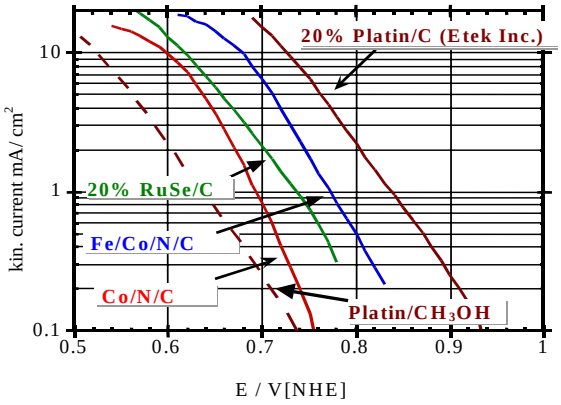

Fig. 2: Tafel plots of Ru-Se/C and Co-Fe-N/C catalysts obtained from rotating disc electrode measurements. Please, note the shift of the platinum curve in the presence of methanol.

Our results show that molybdenum is not necessary in the catalyst composition to obtain an effective four-electron-reduction process of oxygen. Therefore, further experiments were done without any molybdenum. Although even with a selenium free ruthenium catalyst, prepared by thermolysis, oxygen reduction was achieved, addition of selenium increased the catalytic activity and stabilized the catalyst against oxidation. The highest activities were obtained with a Se amount of 14.5 % (related to the content of ruthenium). Further addition of selenium led to a decrease of the activity, may be due to the formation of elementary selenium as it was detected by XRD measurements.

To get a deeper insight into the structure of the Ru-Se catalyst measurements with Thermo-Gravimetry TG, X-Ray Diffractometry XRD, Extended X-ray Absorption Fine Structure EXAFS Analysis, Transition Electron Microscopy TEM and X-ray Photoelectron Spectroscopy XPS were performed.

XRD and TEM measurements revealed that the catalyst prepared from $Ru_3(CO)_{12}$ by thermolysis in the presence of an optimized selenium concentration consists of metallic Ru-particles with a particle size of about 2-6 nm. No other crystalline compounds, such as $RuSe_2$ or RuO_2, could be detected. In TG-measurements, it was found that the samples release considerable amount of the gas species CO and CO_2 (Fig. 3) upon heating in vacuum, which belongs to an amorphous layer covering the metallic

core of the Ru nano-particles. A release of selenium is observed at 800°C and at about 1100°C. However, only the latter led to a decrease of the catalytic activity. To elucidate Ru-Se, Ru-O and Ru-C distances of the amorphous part of the catalyst EXAFS measurements were performed using synchrotron radiation (RÖMO II X1.1 station at HASYLAB) (Fig. 4).

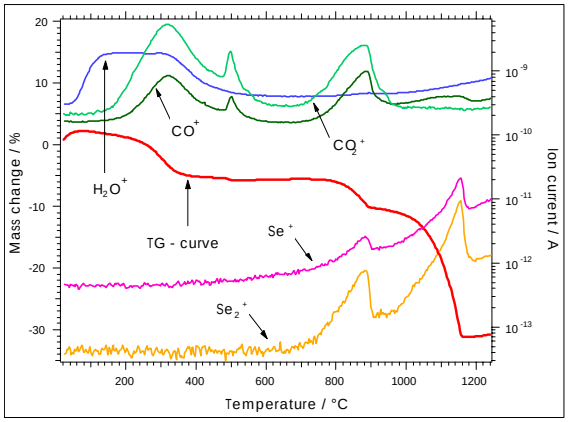

Fig. 3: Thermogravimetric curve of a Ru-Se catalyst heated under argon gas flow. The red curve indicates the stepwise release of CO_2 and CO (200-350°C) and the loss of selenium in a first step as SeO_2 (700-900°C) and in a second step as Se_2 (1000-1200°C).

All Ru-Se catalysts weakly showed the EXAFS pattern of Ru metal and additional features that can be addressed as Ru-Se, Ru-C and Ru-O bondings. Inferring the Ru-Se distance by adjusting EXAFS profiles it was found that the distance in the as grown material amounts to a value of $d_{Ru\text{-}Se} \approx 2.56$Å which is typical for metal organic compounds such as $Ru_4Se_4(CO)_{12}$. The Ru-C and Ru-O distances are 1.95Å and 1.97Å, respectively. This behavior can be explained by the presence of amorphous ruthenium oxides or hydroxides and metal organic complexes covering the surface of the Ru nano-particles.
After annealing of the unsupported catalysts at 450°C and 900°C both distances become close to those found in $RuSe_2$ and RuO_2 and the Ru EXAFS pattern becomes dominant. Obviously the amorphous Ru-oxides were disproportionated to metallic Ru and RuO_2 during the heat treatment step and stoichiometric but catalytic inactive $RuSe_2$ was formed. From XRD measurements it is known that with increasing temperature the unsupported Ru particles coalesce increasing from 4nm to 20nm in size. All this changes led to a decrease of the observed current density obtained from unsupported catalysts after the heat treatment.
During the annealing of the carbon supported samples the amorphous ruthenium oxides and hydroxides were reduced by carbon to metallic ruthenium. Howeve, the Ru-Se distance remained unchanged and no stoichiometric $RuSe_2$ compound could be detected. Additionally, no growth of the particle size was observed. Obviously the ruthenium particles were stabilized by the carbon support.
The observation that the catalytic activity of the carbon supported catalysts can be increased by heat treatment of the catalyst in vacuum, where the most of the surface complexes thermally decompose, might be an indication that the presence of these complexes is sufficient but not necessary to achieve high catalytic activity of the catalyst. However, the modification with selenium led to a chemical stabilization of the metallic ruthenium particles and to a high catalytic activity towards the oxygen reduction.

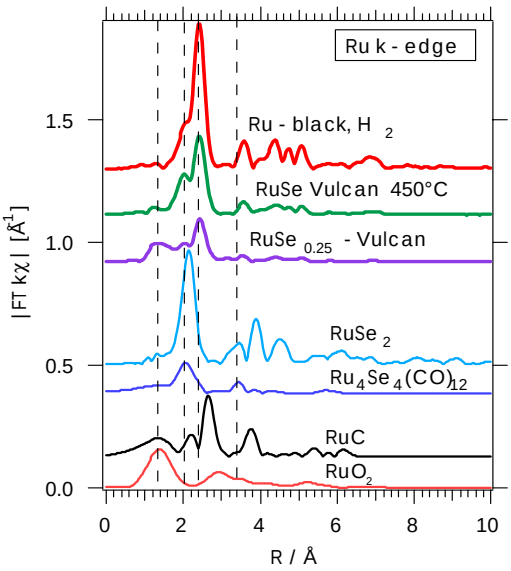

Fig. 4: Fourier transformed EXAFS spectra of as grown and heat treated Ru catalysts in comparison with $RuSe_2$, RuO_2, RuC and Ru_4Se_4 $(CO)_{12}$.

In order to improve the current densities for the application in industrial fuel cell systems three additional methods for the preparation of carbon supported catalysts were developed: formation of ruthenium particles as a precursor by the reduction of ruthenium oxalate (cheap chemical compounds and aqueous solutions), impregnation of carbon black with $Ru_3(CO)_{12}$ (best cost-performance analysis) and the formation of ruthenium colloids as precursor by a micelle technique described by Bönnemann [2] (highest electrochemical performance). The morphology of the different Ru-nano-particle were analyzed by transmission electron microscopy (TEM) and X-ray diffraction (XRD), which shows that the different catalysts consist of crystalline ruthenium particles with a good dispersion over the applied carbon substrate. Smallest particles were found using Bönnemann´s colloidal technique (2.5nm) while the thermolysis method formed particles of 4nm size. Largest particles were obtained using ruthenium oxalate (7nm). Several techniques for the subsequent modification of the Ru-particles with selenium were developed to obtain the high catalytic activity and the chemical stability against oxidation. An increase of the current densities obtained by RDE measurements by a factor of 2 to 3 was found after this treatment.
As expected from the particle size analysis the catalysts prepared by the micelle technique showed the highest current densities. However, with decreasing particle size the apparent overvoltage for the oxygen reduction decreases less significant as expec-

ted from the increase in relative surface area from the respective catalysts. These results suggest that the concentration of surface sites on the carbon substrate, which bond catalytic particles, is limiting the overall current density. Catalysts loading higher than 20 % ruthenium / 80 % carbon did not lead to a further increase of the current density. However, the presence of selenium was found to have a significant effect on current density and may act as an electron transfer bridge between substrate and catalytic center. Furthermore, the surface of the ruthenium nano-particles is chemically modified by selenium and become stable against oxidation.
In co-operation with DaimlerChrysler/Ulm these optimized catalysts were used to prepare Gas Diffusion Electrodes GDEs and Membrane Electrode Arrays MEAs for the application in PEM fuel cells. Fig. 1 shows some results obtained from fuel cell measurements.
Nevertheless, under the best conditions achieved the overvoltage obtained from our catalysts by RDE and fuel cell measurements in alkanol free acid media is approximately 0.12 V higher than for a comparable platinum catalyst. This could be explained by an activation barrier for the overall oxygen reduction that is approximately 0.15 V higher than for platinum.
However, in the presence of alkanols the Ru-Se catalysts is more effective than platinum (Fig. 1). Therefore, it could be used in DMFCs or as a sensor-material for oxygen in alkanol containing media. Both applications are still under investigation.

Iron-cobalt based catalysts

Iron-cobalt catalysts were prepared by pyrolysis at 840°C under argon atmosphere using a mixture of cobalt tetramethoxyphenylporphyrin (CoTMPP), as a nitrogen-containing organic transition metal complex, and iron oxalate ($Feox_2$). During the heating process, $Feox_2$ first releases water prior to decomose into FeO under CO_2 and CO gas evolution. Melting and decomposition of CoTMPP occurs in the same temperature range (250-500°C). At 900°C the pyrolytic reaction is completed. Carbon, generated during the decomposition of CoTMPP, reduces FeO particles to metallic iron. After cooling the sample, the iron particles were removed by etching in an acidic solution. SEM and TEM images reveal that this procedure led to an in situ generation of carbon black with a very high porous structure (Fig. 5).
According to the literature it is assumed that the catalytic centers consist of metal atoms integrated into the surfaces of the carbon support by pyridinic-type nitrogen. Even after the complete removal of metallic iron, a residual amount of iron was found by EXAFS, Energy Dispersive X-ray EDX analysis and Neutron Activation Analysis NAA in the samples. Obviously, beside the cobalt atoms also a small amount of iron atoms are incorporated into the carbon structure. From EXAFS measurements a Co/Fe ratio = 20:1 and a Co-N distance of 1.97Å were inferred.

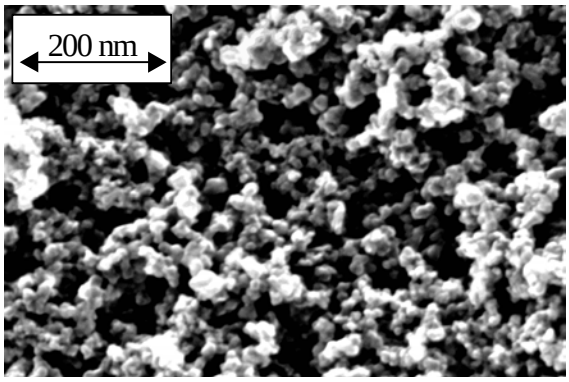

Fig. 5: SEM image of the porous Co-Fe-C catalyst prepared from Co TMPP and $Feox_2$ by pyrolysis.

The Tafel-plots obtained by RDE measurements reveal the high catalytic activity of the Co/Fe samples, which comes close to that of the Pt-standard. Interestingly our Co/Fe catalysts yielded higher current densities than a comparable sample prepared from CoTMPP without any iron (Fig. 2). Further investigations have to clarify if this is due to the incorporated iron atoms or to a morphological effect caused by the decomposition of the iron-oxalate.

References

[1] Solorza-Feria, O.; Ellmer, K.; Giersig, M.; Alonso-Vante, N.: Novel Low-Temperature Synthesis of Semiconducting Transition Metal Chalcogenide Electrocatalyst for Multielectron Charge Transfer: Molecular Oxygen Reduction. Electrochim. Acta 39 (1994) 1647.

[2] Bönnemann, H., Brijoux, W., Brinkmann, R., Dinjus, E., Joußen, T., Korall, B., Angew. Chem. 103 (1991) 1344-1346.

M. Hilgendorff, M. Bron, H. Schulenburg, I. Dorbandt, P. Bogdanoff, S. Fiechter, H. Tributsch (SE5.01b Platnium-free Catalysts for the Reduction of Oxygen in Fuel Cells)

Interface engineering

The project aims at optimization of optoelectronic properties of semiconductor interfaces and at directed band alignment in semiconductor heterocontacts by (photo)electrochemical and chemical techniques. This includes the investigation of structure formation phenomena induced by electrochemical treatments. Accompanying photoelectron spectroscopy and in-situ/ex-situ scanning probe microscopy investigations serve for the understanding of the reaction mechanisms occurring during the interface modifications. Priority objectives are

- development and optimization of photoelectrochemical, electrochemical and chemical processes for the surface conditioning of relevant photovoltaic materials;
- electrochemical preparation of alternative buffer layers;
- influencing the band alignment by adsorption of atoms, ions and molecules;
- investigation and influencing of self-organized and scanning probe microscopy induced structure formation for light-coupling systems and photonic structures.

The investigated materials were $CuInS_2$, Si and InP.

The original electrochemical method for the removal of deleterious CuS from Cu-rich prepared CIS surfaces was further developed and simplified (two electrochemical steps instead of three). The new procedure for replacement of the KCN etch by non-toxic electrochemistry is based on a transformation of CuS to Cu_2S and its partial dissolution in alkaline solutions; addition of small amounts of In ions to the electrolyte leads to a removal of CuS and Cu_2S.

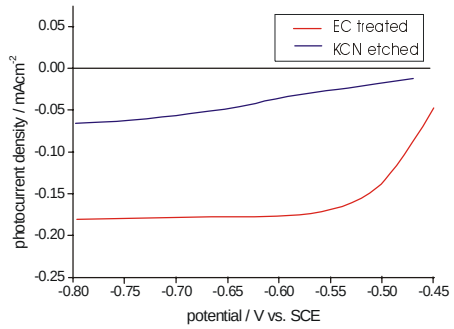

Fig. 1: Photocurrents obtained for an electrochemically (EC) treated and KCN etched CIS sample in S^{2-}_x/S^{2-} redox electrolyte.

In redox electrolytes, the photocurrents obtained for electrochemically prepared samples are now larger than for KCN etched samples (Fig. 1). The electrochemical reduction of CuS to Cu_2S is confirmed by XPS measurements: the Cu line has shifted to the value for Cu in Cu_2S. In addition, a pronounced decrease in the FWHM for S and a simultaneous decrease in the FWHM of Cu indicate a reduction of the different bonding sites after the transformation. The addition of small amounts of In ions to the solution leads to the dissolution of CuS and Cu_2S and obviously also to a chemical change of the CIS surface: after the treatment, the Cu and In lines correspond to the respective line positions in CIS while the S line position is located at a binding energy lowered by 1 eV compared to the S line position in CIS. From this and the intensity ratios of the Cu, In and S lines, a coverage of CIS with a few ML of an In-S phase can be concluded. The chemical surface change also affects the valence band position relative to EF, as obtained with synchrotron radiation: $E_F - E_V = 0.9$ eV ($E_F - E_V = 0.5$ eV for KCN etched samples).

The investigation of alternative possibilities for directed structure formation at silicon surfaces necessitates fundamental studies of dissolution at a molecular level. In the acidic processing regime, the divalent dissolution leading to porous Si can be induced by holes, for instance in n-Si under illumination. We have found, however, that pit formation leading to porous structures occurs also on highly n-doped Si in the dark at neglegible hole concentration (Fig. 2). So far, no plausible explanation for this finding has been given. In a sytematical study using variably doped n^+-Si

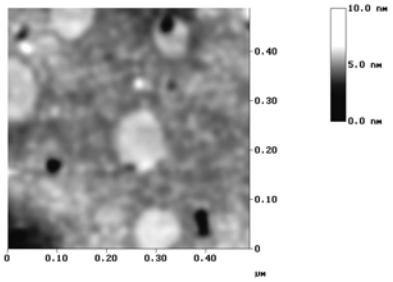

Fig. 2: In-situ AFM micrographs of n-Si (111) ($N_D = 2 \cdot 10^{18}$ cm^{-3}) obtained after reaching the first dark current maximum.

we observe that for decreasing doping level the current onset connected with por-Si formation is shifted towards anodic potentials. It is found that the relative potential drop in the Helmholtz layer always amounts to the same value of 0.5 V. The shift of the current onset is interpreted by assumption of an interface state 0.3 – 0.5 eV below the conduction band edge, extending some Å into the Helmholtz layer. The state is shifted energetically proportional to the potential drop ΔV_{HH} in the Helmholtz layer. For sufficiently large ΔV_{HH} electron injection becomes possible (Fig. 3). Since the injected electron is delocalized in the conduction band local corrosion is assumed as a result of subsequent chemical steps. Either surface atoms are attacked by decomposition products of the oxidised surface complex (radicals) and/ or bond rupture results in local dissolution of Si atoms.

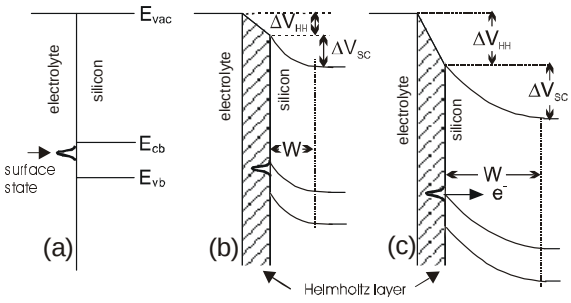

Fig. 3: Energetic position of the suggested surface state; (a) flatband condition; (b) anodic polarization; (c) electron injection.

Investigation of electrochemical processes with synchrotron radiation

Photoelectron spectroscopy investigations related with the project, which cannot be carried out with the necessary degree of resolution and surface sensitivity by use of common XPS/UPS systems are performed with synchrotron radiation at BESSY (cooperation with the Cooperating Research Group (CRG)).

In the search for self-organized and SPM induced microtopography alterations, initial phases of por-Si formation in dilute ammonium fluoride solution were investigated by synchrotron radiation and AFM. Fig. 4 shows AFM data for the Si(111):H(1x1) surface (Fig. 4a) and in Fig. 4b the onset of pit formation at step edges of atomic terraces after anodic processing at + 0.1 V from the rest potential.

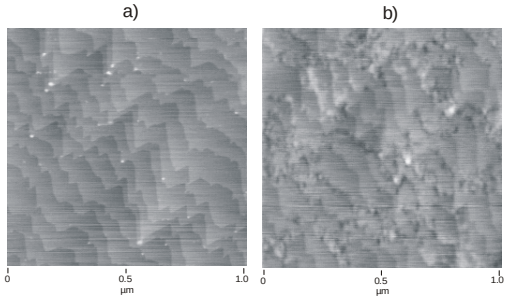

Fig. 4: AFM images of a Si(111) surface (a) before and (b) after initial corrosion reaction

Fig. 5 displays PES data obtained after emersion close to the first photocurrent maximum where divalent dissolution still takes place. Five features are discernible: the core level signal (signal A), a surface core level shift indicating residual H-termination (0.35 ML; signal B) and mainly two oxidized species shifted by 1 eV (C) and 4 eV (E). The former is attributed to a = Si-H-F species. DFT calculations yield a Si partial charge of $\rho = 0.54$ for the = Si-H-F species. Signal D is too small for serious evaluation; signal E can only be evaluated under consideration of the O 1s and F 1s lines (not shown). The former shows O in OH^- and H_2O but not O in SiO_2. The latter shows predominantly F in $Si\text{-}F_x$. In conjunction with DFT calculations we attribute the 4 eV shifted signal to $SiOHF_3$, a precipitate from the dissolution reaction. The presence of species C indicates that solvolytic splitting of backbonds is rate determining, possibly due to the complex chemical reactions involved.

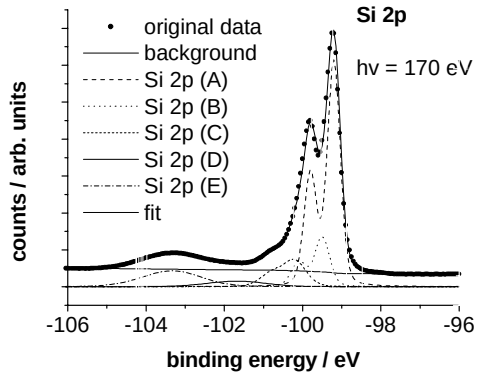

Fig. 5: Si 2p line after sample emersion at the first current maximum in the i-V characteristic (cf. Fig. 7) including deconvoluted signals.

H. J. Lewerenz (SE5.02 Surface Engineering), M. Aggour (guest scientist), C. Murrell, H. Jungblut, M. Kanis, J. Jakubowicz (DFG Priority Program: Fundamentals of Electrochemical Nanotechnology)

Work Group

SE6 Electronic Structure of Semiconductor Interfaces

TGM7, Transfer of a VUV monochromator to a BESSY II dipole beamline

With closing of BESSY I in 1999 it was decided to transfer the monochromator TGM7 to BESSY II. The instrument was used for the characterization of semiconductor interfaces and the electronic structure of materials relevant for solar energy conversion. The TGM7 had been designed in 1988 to deliver photons in the range of 6-120 eV with a resolution of about 250 meV and reasonable intensity in a photoemission experiment. To cover the photon energy range two gratings are installed ranging from 120-16 eV and from 30-6 eV.

Fig. 1: Location of TGM7 at BESSY II

With the transfer the beamline had to be adapted to the new dipol and the beam characteristics at BESSY II. Due to the lower ring current a focussing mirror of ca. 500x220 mm was chosen and the angle of incidence was decided to be slightly smaller. It was suggested to gain a little in resolution by maintaining about the same intensity as at BESSY I.

Fig. 2: Focussing mirror, cooling facilities and mechanics installed in the new vacuum chamber.

With the new focusing mirror the beamline from the outlet system up to the slit section of the monochromator had to be redesigned. Especially a completely remote controlled mirror adjustment of all 6 degrees of freedom had to be realized. Within two years the design and fabrication of the chamber, the mechanics, and the prefabrication of the mirror substrates took place. In December 2001 after installing the components and preadjusting the optics, for the first time the beamshutter was opened. Severe outgasing of the new components hidden by the intense white synchrotron light restricted the first operations to low ring currents. After the final adjustment of the focussing mirror by the help of the motor driven mechanics was achieved and first spectra were taken. Fig. 3 displays the transmission spectrum of an Al foil in the range of the LII/III edge. The resolution obtained here with 100 µm slits was at BESSY I only obtained with much smaller slits (50 µm, hence lower intensity), showing nicely the improvement in resolution. A resolving power of $E/\Delta E = 880$ was reached for 20 µm slits, the limit of the instrument.

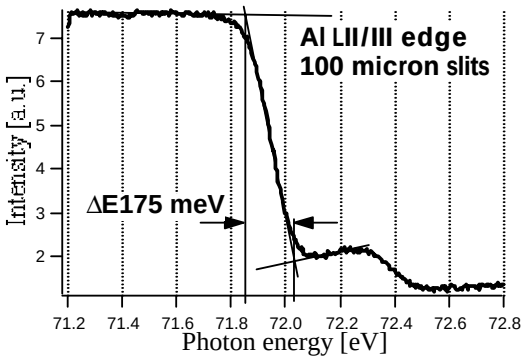

Fig: 3. Absorption spectrum of an Al foil at the LII/III edge

Far more important are the obtained photoemission spectra as an overall resolution of about 200 meV for monochromator and electron spectrometer for an Al2p core level were obtained at 95 eV photon energy.

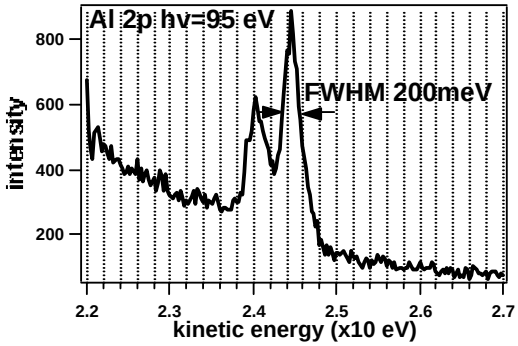

Fig. 4: Photoemission of Al 2p level

The yield curve of the instrument will give an intensity of a factor 2-3 above the value reached at BESSY I, normalized to 100 mA ring current. As the maximum current at BESSY II is about a factor 3 lower, the overall intensity is of the same order as obtained at BESSY I.

C. Pettenkofer, S. Tiefenbacher
(SE6.01: Electronic Structure of Semiconductor Interfaces)